A Study of the Energy Efficiency of Various AA Batteries

David Cruz Lopez, Enrico Ruffolo, Oishee Nandy, Lavanya Upadhyaya
PHYS 398 DLP | Professor George Gollin | Fall 2020

Abstract

The aim of this project was to investigate the energy efficiency at different temperatures of three different types of AA batteries: Nickel Cadmium (Ni-Cd), Nickel Metal Hydride (Ni-MH), and Lithium Ion (Li-Ion). This effect was quantified by measuring the ratio of energy transferred when charging and discharging the battery. Energy ratios were collected for each battery at room and cold temperatures to examine differences in performance. The reliability of the results was established through examination of the collection equipment, such as the INA219 current sensor. Plots of energy ratios and currents as functions of temperature and battery type illustrated each battery's efficiency, explaining power dissipation due to internal resistance, particularly for the Lithium-Ion battery. The data and respective plots suggest that temperature has a significant effect on the performance of rechargeable batteries, but the magnitude of the effect depends on the battery type.

---

1 Introduction To Batteries

Chemical reactions require specific conditions to happen spontaneously. Understanding the chemical processes that occur within batteries can provide insight into the expected energy efficiency of batteries at specific temperatures.

Batteries are the composition of one or multiple electrochemical cells. Electrochemical cells are composed of three basic components: an anode terminal ('-'), cathode terminal ('+'), and electrolyte chemical substance. When both terminals are connected in a circuit, the electrolyte undergoes a spontaneous chemical reaction between the anode and cathode allowing electrical current to flow. The electrolyte works as a medium through which electrons are transferred. This process results in corrosion of the anode metal. These reactions complete or diminish when the terminals electrochemical potentials equate, the anode is completely depleted, or the cathode becomes completely plated with the anode material.

Cells can be described as galvanic or electrolytic. A galvanic cell derives energy from spontaneous redox reactions taking place between the anodes and cathodes, while an electrolytic

cell utilizes energy to perform non-spontaneous redox reactions (Libretexts, 2020). Primary batteries have solely galvanic cells, meaning the reaction utilized to generate electrons at a higher potential is not reversible. Secondary batteries, such as rechargeable batteries, can reverse the reaction by applying a potential to the cathode which restores the anode (Hymel, 2020). All three of the batteries within this report are secondary batteries, and therefore rechargeable.

Rechargeable batteries are extremely useful for different applications. They are especially prominent in common consumer products such as laptops, smartphones, powertools, and vehicles, but their applications are continuously growing. Moreover, specific battery types have different chemical and mechanical properties that allow them to be used in different situations and environments. Specific battery designs may vary in voltages, ways of charging, recommended working conditions, and expected life spans.

As the aim of this project is to test the energy efficiency of AA batteries in different conditions, three types of common rechargeable batteries, Ni-Cd, Ni-MH, and Li-Ion, will be used to perform the analysis. Figure 1 shows the various batteries used to collect data in this report. Although the size and chemical compositions of the batteries are specified, differences in the internal design will have considerable effects on the battery's performance. The battery manufacturers displayed in Figure 1 show which batteries were used to collect data.

Figure 1*: Various batteries used for data collection. Left: Nickel Cadmium. Center: Lithium Ion. Right: Nickel-Metal Hydride*

Depending on the chemical makeup and internal design of the battery, there are limitations on the amount of current the battery can operate at. In most cases, safe charging and discharging values are given as a ratio of battery's capacity per hour. For example, a battery charged at C/20, where C is the battery capacity, shows that the charging process takes 20 hours. In the case of discharging, this can correspond with a specific current value. However, this does not necessarily correspond with a specific charging current or rate of power transfer as will be shown in Section 3.2. As specific batteries operate more efficiently in specific conditions, the test procedure will be standardized over a range which includes optimal and non-optimal conditions. As non-optimal conditions can cause irreparable damage to a battery, it is important to note that a new battery is used to collect data for each set of conditions.

AA Batteries

AA batteries are single cell cylindrical batteries that have a length of 49.2–50.5 mm and diameter of 13.5–14.5 mm. Similarly, it is required that the nominal voltage across the terminals of the battery is 1.2-1.5 volts. The nominal voltage of a cell is the voltage difference between the terminals when fully charged.

For the batteries used, specifications regarding their operation are listed below. The capacity is given in units of mAh, which demonstrates the amount of current which can be supplied for a unit time. For example, a 1500 mAh battery can supply 500 mA for 3 hours or any current, I, for C/I hours. Since Li-ion cells supply a voltage much higher than the typical AA battery, they require regulators to ensure the cell voltage is within the required range.

Battery	Nominal Voltage per cell (V)	Operating Temp Ranges: Charge (°C)	Operating Temp Ranges: Discharge (°C)	Battery Capacity (mAh)	Charge/discharge efficiency (%)	Charge rate (Capacity)
Li-Ion	3.6-3.8	0°C to +45°C	-20°C to +60°C	1500	80% - 90%	C/5
Ni-Cd	1.2-1.45	0°C to +45°C	-20°C to +65°C	600	70% - 90%	C/10
Ni-MH	1.2	0°C to +45°C	-20°C to +65°C	2000	66% - 92%	C/10

Figure 2*: Information on nominal voltage, operating temperatures, and charging specifics from different manufacturing sites on the various types of batteries used. Data was collected from different articles in (Battery University, 2017)*

To give a better understanding of the chemical composition of each battery, the following sections give a detailed description of their internal processes and intended uses.

Lithium Ion

American physical chemist G.N. Lewis pioneered the development of the Li-Ion battery in 1912, but the first non-rechargeable Li-Ion battery was made commercially available only in the early 1970s (Battery University 2017). Li-Ion batteries are constructed from two positive and negative electrodes separated by a liquid chemical electrolyte, such as diethyl or ethylene carbonate. Lithium has the greatest electro-chemical potential and provides the largest energy density despite being the lightest of all gasses.

Lithium ions (Li+) are part of the chemical reaction process that drives batteries. The electrodes in a lithium-ion cell are composed of materials that can intercalate these ions. Intercalation occurs when the charged ions of an element can be contained inside the structure of another host material without causing chemical disruptions. In the case of a Li-Ion battery, the lithium ions can be described as 'tied' to an electron within the anode. When the battery discharges, the intercalated lithium ions are released from the anode, when they then travel through the electrolyte solution to be absorbed in the cathode (Clean Energy Institute, University of Washington 2020).

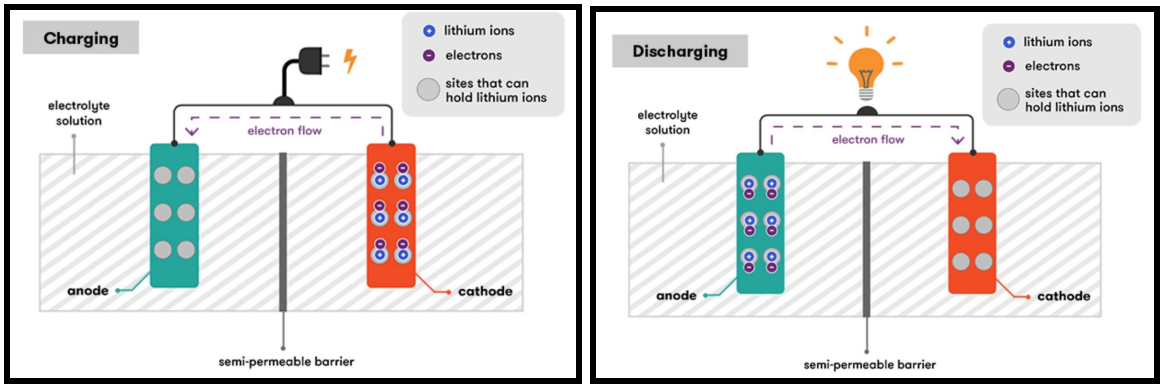

Figure 3 *: Lithium Ion charging and discharging.*
Images from (Bhatt, Wang, Withers. Australian Academy of Science 2017)

A Li-Ion battery typically begins in a state of full discharge, as all the ions are intercalated in the cathode, which results in the battery's chemistry not having the ability to produce any electricity. As the battery is charging oxidation occurs, meaning that the cathode loses electrons. In order to maintain a charge balance in the battery cell, some positive ions are introduced and dissolved in the electrolyte solution. These positive ions travel to the anode where they are intercalated with the graphite. This intercalation reaction deposits electrons into the graphite anode to 'tie' up the lithium ion. When the battery begins to discharge, lithium ions are de-intercalated from the anode and travel back through the electrolyte to the cathode. This releases electrons that were attached to the anode and allows them to flow through an external circuit providing current which can be used to do work. The battery is then no longer able to push current when the cathode becomes plated with lithium ions. In order to recharge the Li-Ion batteries, an electric current must be applied to push lithium ions back to the anode from the cathode (Bhatt, Wang, Withers. Australian Academy of Science 2017).

Li-ions batteries typically have built-in regulators to prevent damages such as overheating, complete discharge, and overcharging (Chu, Z., et al. ScienceDirect 2019). Overcharging a Li-ion battery can result in permanent damage and eventually catastrophic failure due to lithium plating which forms when reaching high voltage values. In addition to the required

regulators, Li-ion batteries may contain venting caps to prevent cells from rupturing or to maintain safe voltage levels (Bhatt, Wang, Withers. Australian Academy of Science 2017).

Lithium-ion batteries work well in various systems and environments due to their high power density, lightweight, long lifespan, and thermal stability. For example, Li-Ion batteries are used in electric vehicles and marine motors due to their reduced weight and size when compared to conventional lead acid batteries. Additionally, the fast and resistance charging behavior of Li-Ion batteries collects solar power more efficiently (ReLiON, 2015).

Nickel Cadmium

Nickel–Cadmium batteries have high power density and energy efficiency, and have been deployed in electric vehicles up to the 1990s. These devices use a Nickel Dioxide (NiO_2) cathode and Cadmium anode, with a Potassium Hydroxide (KOH) electrolyte. More specifically, the batteries discharge two compounds, $Ni(OH)_2$ and $Cd(OH)_2$, from the cathode and anode respectively. The KOH alkaline solution serves as the electrolyte during the discharging process (Abdin, Khalilpour, 2019).

The electrochemical equation for the spontaneous reaction in Ni-Cd battery cells is as follows: $Cd\ (s) + NiO_2\ (s) + 2H_2O \leftrightarrow Cd\ (OH)_2\ (s) + Ni(OH)_2\ (s)$, where (s) denotes a solid element or chemical compound. During charging, this reaction goes from right to left.

Due to the chemical processes in Ni-Cd batteries, these batteries are sometimes fitted with pressure valves that allow the release of gasses created in operation prior to cell rupture. They are typically vented when large capacities or discharge rates are required. In the case of AA batteries, Ni-Cd batteries are not vented.

Nickel-based batteries differ from Lithium batteries in a couple of ways. The over-charging of the Nickel-Cadmium battery typically helps a charger recognize that a battery has been completely charged. As a result, the voltage cutoffs of Li-Ion battery charger circuits are strict in comparison to nickel-based battery chargers. Moreover, the nickel-based batteries typically have a more complex charging procedure than the Li-ion batteries. Nickel-based batteries allow the voltage to rise freely, but they are charged with a pulsing current. This will be covered in Section 3.2. It is dangerous to short-circuit Ni-Cd batteries since it can cause excessive heat and loss of hydrogen gas, which can cause serious damage to the battery and its surroundings. Ni-Cds can typically charge at 115% of their total capacity while maintaining minimal reduction in lifespan, making them ideal for heavy duty power jobs. These batteries are also known for their ability to maintain capacity and natural discharge rates in cooler conditions.

Nickel-metal hydride

Nickel-Metal Hydride (Ni-MH) batteries, patented in 1986 by Stanford Ovshinsky when researching materials for storing hydrogen, have a 1.5 to 2 times higher energy density than Ni-Cd, even though they generally take longer to charge due to a different chemical makeup. These batteries are inter-conversion type devices, meaning that they have a low risk of explosion, and exhibit high power capability, environmental compatibility and safety, and tolerance to overcharge and over-discharge (Encyclopedia of Electrochemical Power Sources, 2009). Ni-MH has also become the dominant advanced battery technology for use in electric and hybrid-electric vehicles due to its design flexibility and safety (Alternative Fuels and Advanced Vehicle Technologies for Improved Environmental Performance, 2014).

Nickel-metal hydride batteries have a high metal content, consisting of a nickel oxide cathode, interstitial metal oxide anode, and potassium hydroxide alkaline electrolyte. The metal hydride anode is a metallic alloy that captures hydrogen at nearly a thousand times its own volume (Energizer Brands, LCC, 2020). The overall cell reaction is as follows:

$M + Ni(OH)_2 (s) \rightarrow MH + NiO(OH) (s)$, where "M" is the intermetallic alloy capable of forming a metal hydride phase. As seen in the equation, Mi-MH electrochemical reaction involves the transfer and insertion of the H^+ cation.

The Ni-MH battery is a variation of the nickel-hydrogen battery. Since metal-hydrides corrode when exposed to KOH, they lose stored energy quicker than nickel-hydrogen batteries. Nickel-hydrogen batteries use the same NiO_2 cathode and KOH electrolyte as the Ni-Cd batteries. Nickel-Metal Hydride batteries are not likely to fail catastrophically, as overheating or improper venting only leads to ruptured cells. Since the content of these batteries can reach high temperatures, burning surrounding materials is the largest risk upon battery failure.

2 Methodology

The methodology section documents the data system's design and development. To achieve the project's goal, a microcontroller was used to record data from sensors placed within circuits to collect the battery's current and voltage when charging and discharging. The sensors and microcontroller were supplied, meaning that there was little research into better alternatives.

To better understand the Arduino Mega 2560 microcontroller and Adafruit sensors, a breadboard was used to connect the microcontroller to the devices and sensors. The Arduino Integrated Developer Environment (IDE) and libraries were used to test and verify each sensor's properties and functions. Similarly, a protoboard was used to develop a circuit which allowed the test battery to switch between being connected to the charger and load. Gathering discharging data was simple, as a current sensor could easily be placed in series with a precision resistor. A "fake" battery, designed by a 3D printer with metal terminals on each end that replicated a battery, was used to gather data on the battery charger's functions. By connecting wires to these terminals, a sensor could be placed in series with the test battery. The "fake" battery completed a loop in the circuit, acting as a placeholder and connecting the charger to the proto board. As a result, placing the fake battery in the charger allows current to flow from the charger to the test battery, where the INA219 can begin data collection. Please refer to Figures 14 and 15c for visuals of the fake battery and a circuit schematic of the PCB and protoboard. After understanding the IDE and required circuitry, the Autodesk EAGLE software was used to create a schematic for a printed circuit board (PCB).

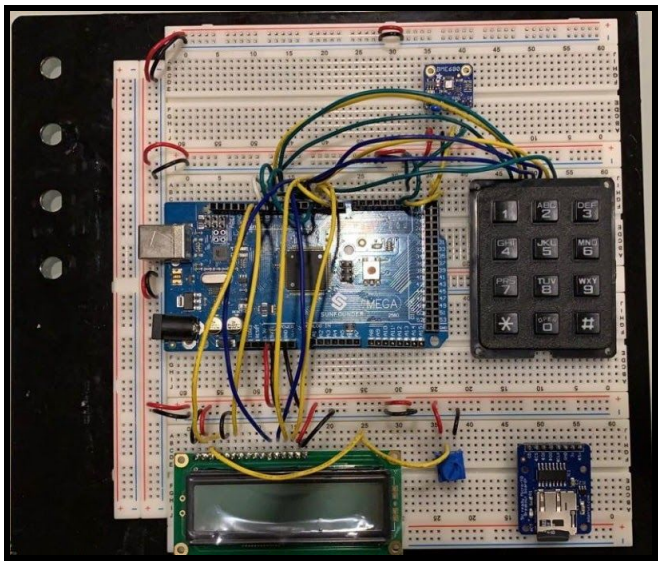

Figure 4*: Breadboard with relevant components: Arduino Mega2560, keypad, BME680, LCD display, potentiometer. Note: Not all necessary wires and sensors are present within this image. For a better understanding of the circuit, please refer to the schematic.*

2.1 Instrumentation

This section covers an in-depth overview of the microcontroller and sensors used within the PCB. Any data values used from each component were obtained from the Arduino and Adafruit website datasheet.

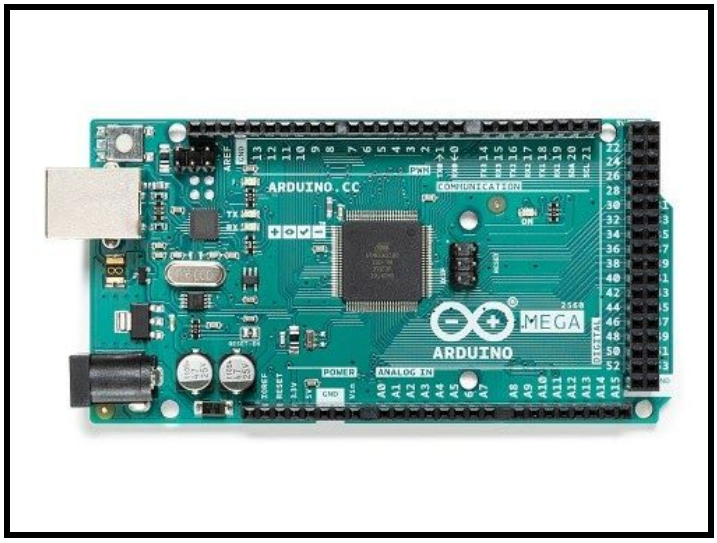

***Figure 5**: Arduino Mega 2560*

- A microcontroller board powered by connecting it to a computer using a USB cable, with a battery or an AC-to-DC adapter. The microcontroller establishes circuit connections and communications with all devices and sensors wired to it, allowing data collection from multiple sources using I2C protocol and recording them in a single text file. Some of the relevant specifications are as follows:

Microcontroller	ATMega 2560
Input voltage (recommended)	7 - 12V
Operating voltage	5V
Digital I/O pins	54
Analog Input Pins	16

***Table 1**: Data values for Mega 2560*

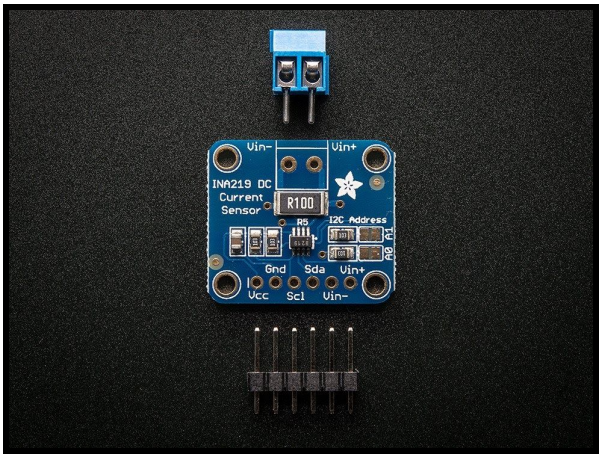

***Figure 6**: Adafruit INA219*

- 2 Adafruit INA219 Sensors

The INA219 current sensor measures the high side voltage (shunt and load) and DC current with a precision of 1%. High side voltage refers to the voltage it is receiving as an input. In this case, the test battery provides the high side voltage.

To collect data on the charging and discharging of a battery, an INA219 current sensor was placed in series with the battery and load using the fake battery described above. This sensor collects data by allowing the load current to run through a 0.1 ohm shunt resistor. The voltage drop across the resistor is how current is approximated. This voltage is decoded by a 12-bit ADC, which gives the INA219 a resolution range of 0.8 mA and a maximum current reading of 3.2 Amps without modifications. However, the shunt resistor proved to be problematic as the internal resistances of these battery types tend to be significantly lower than 0.1 ohms. As the INA219 is in series with the test battery, the charger interprets the entire loop's resistance as internal resistance. With the increase in the apparent internal resistance, all chargers gave error readings. To accommodate for this, the INA219 shunt resistor ran in parallel with a 0.001 ohm resistor. This modification decreased the shunt resistance to 0.00909 ohms, scaling the values by 1/11 and increasing the resolution to 8.8mA. Therefore, every measurement has a quantization that can lead to approximately 3% error.

  - INA219 #1: Used to monitor the current, voltage (shunt and load), and power of the 5*AA batteries on the PCB.
  - INA219 #2: Used to monitor the current, voltage (shunt and load), and power of the test battery on the proto board. This INA219 was in series with a load of 2 10-ohm precision resistors. These resistors were in parallel, giving an effective resistance of 5 ohms. The shunt resistor was approximately $\frac{1}{110}$ ohms after modifying the INA219. Its specifications are as follows:

Operating voltage	3 - 5 V DC
High side Voltage (maximum)	26 V DC
Current sense resistor	0.1 ohm 1% 2W
Maximum Current Measurement	±3.2A (±0.8mA resolution)
Modified Current Sense Resistor	0.0909 ohm 1% 2W
Modified Maximum Current Measurement	±35.2A (±8.8mA resolution)

***Table 2**: Data values for INA219*

***Figure 7**: Adafruit BME680 sensor*

- Adafruit BME 680 Sensor: For measuring physical factors such as temperature, atmospheric pressure, and humidity to report ambient conditions the batteries were exposed to. Its specifications are as follows:

Temperature Precision	±1.0°C
Humidity Accuracy Precision	±3.0%
Barometric Pressure Precision	±1hPa
Operating Voltage	3.3V to 5V
Voltage regulator	3.3V

***Table 3**: Data values for B680*

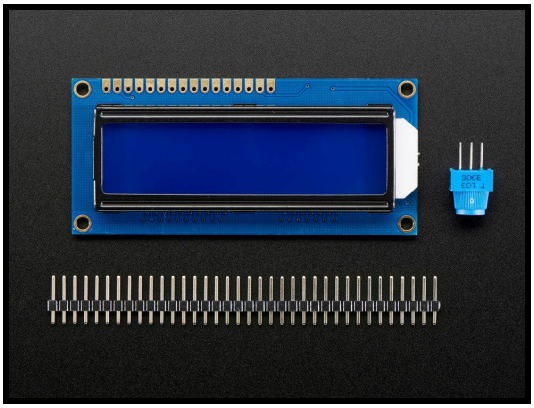

***Figure 8**: Adafruit 16X2 LCD*

- 16X2 LCD display (left): Used to display menus within the testing program, as well as the data being collected. The LCD made the monitoring of the test procedure and battery conditions easier, and ensured that the devices functioned according to expectations.
- 10kΩ Trimpot (right): a three terminal variable resistor used to control the LCD contrast.

Operating Voltage (LCD)	5.0V
Operating temperature (LCD)	-10°C to +60°C
Resistance (trimpot)	10kΩ
Power (trimpot)	0.5W
Tolerance (trimpot)	±10%

***Table 4**: Data values for 16X2 LCD*

***Figure 9**: 3X4 Keypad*

- 3X4 keypad: Used to input the selections for the battery and test type to call the appropriate functions in our data acquisition system explained in Section 2.3.

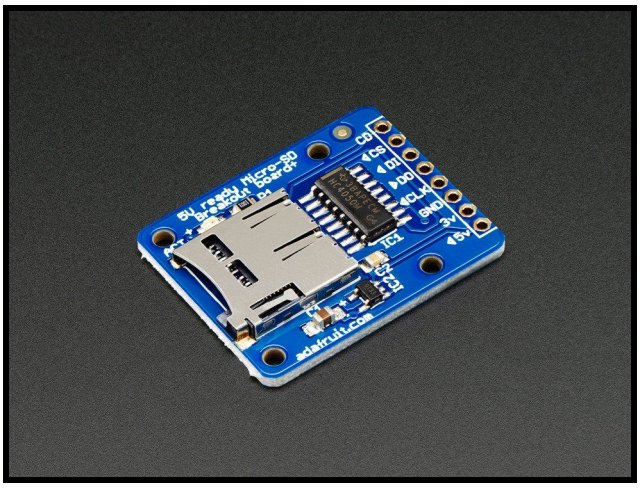

***Figure 10**: Adafruit Micro-SD card reader*

- Micro-SD board and card: Used to read, write, and save data collected from INA219 and BME680 sensors.

Operating voltage	2.7 - 3.6 V DC
Operating Temperatures	-25°C to +80°C
Power up time	250 ms

***Table 5**: Data values for Micro-SD reader*

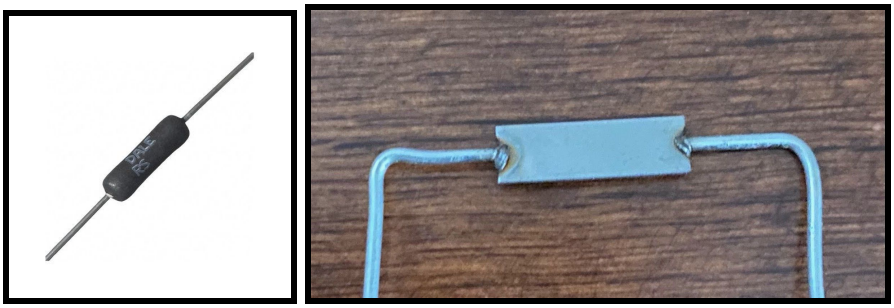

***Figure 11**: Two different types of precision resistors. Image on the right was used during testing*

- Precision Resistors

The accuracy, precision, and resistive temperature coefficients of precision resistors make precision resistors reliable for discharges over long periods of time. These resistors modified the INA219 and discharged the battery. To discharge the battery, two 10 ohm resistors, displayed on the left, were used in parallel. The 0.001 ohm resistor used to modify the INA219 is shown on the right.

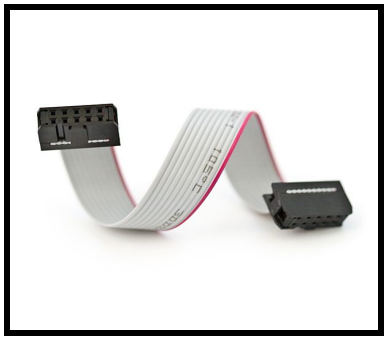

***Figure 12**: Ribbon cable used to connect protoboard to PCB*

- Ribbon cable connectors: As both INA219's are located on the PCB, as shown in Figure 5, a ribbon cable was used to connect the proto board and INA219 for the test battery measurements.
-

***Figure 13**: Types of battery chargers used for testing*

- Battery chargers: POWEROWL Ni-Cd Charger, AmazonBasic Ni-MH Charger, and DeleePow Li-Ion Charger. Each of these are smart chargers, meaning there is internal circuitry that helps dynamically determine how to charge the battery. These circuits use different inputs as a means of adjusting the charging cycles. The inputs and adjustments are discussed in Section 3.2.

2.2 Implementation

The following describes the circuit diagram for the PCB and proto board, which use the sensors and microcontroller mentioned above. As the wiring can change depending on the code within the Arduino IDE, the wire connections will not be explained. For more information regarding the rationale behind the wiring connections shown, please refer to the Adafruit Libraries for the specific sensors and George Gollins Schematics on the Physics 398 DLP course website.

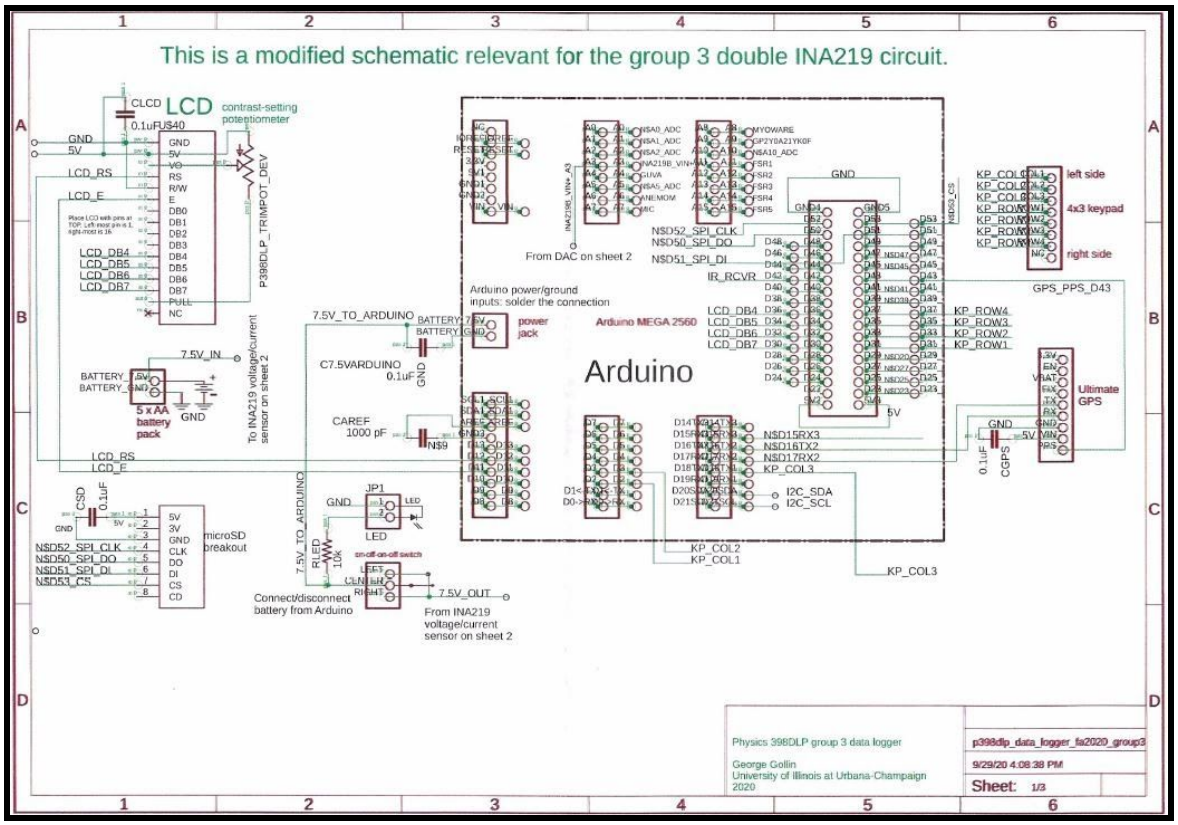

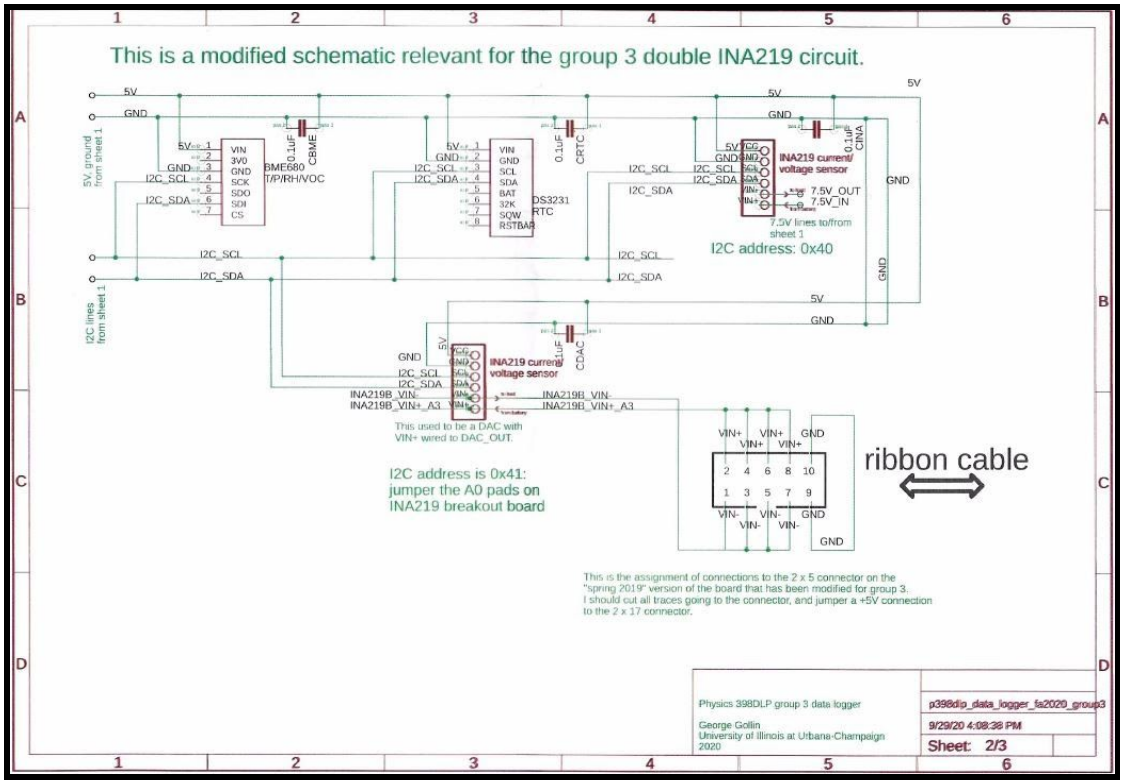

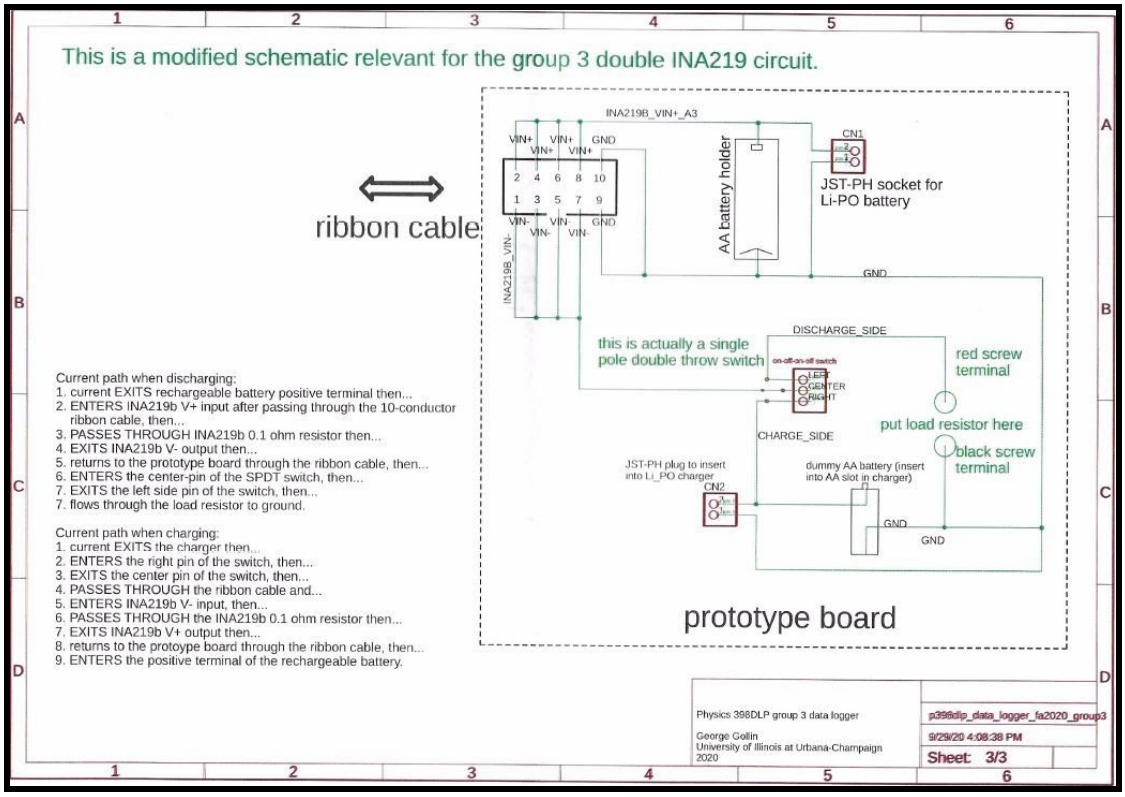

***Figure 14**: Schematic of PCB circuit specific for this project*

The electronic components and Arduino Mega 2560 were soldered and fastened together onto a PCB. A 3D-printed case was created to protect the circuit while in use. Note: The GPS and DS 3231 (I2C real time clock) shown in the following schematic, generated by George Gollin, were not used.

Page 1 in Figure 14 shows that the Arduino receives power from a battery pack toggled by a switch. The state of the circuit is indicated by an LED. The keypad, LCD, and microSD are connected to the Arduino through required ports. Page 2 of the schematic shows the BME 680 and 2 INA219's which have multiple required connections to the Arduino in Page 1. Also, there is the indication of a ribbon cable, which originates at the protoboard. This ribbon cable allows for the INA219 to gather data on the test battery. As the measurements are not incredibly time sensitive, nor require even sampling, the DS 3231 real time clock and GPS (Page 1) are not used. Finally, Page 3 of the schematic demonstrates the layout of the protoboard, as well as the ribbon cable connection. The test battery is connected to a switch which alternates between a loop with the charger or precision resistors. These two loops represent the discharging and discharging circuits. In both cases, the INA219, which is connected via the ribbon cable, is in series with the test battery, allowing for data to be collected. As a result, one INA219 collects data on discharging and charging. As the INA219 does not change orientation within the circuit, the current values will be positive and negative depending on the direction of the current. The following are images of the PCB and protoboard which are created in accordance with the schematics.

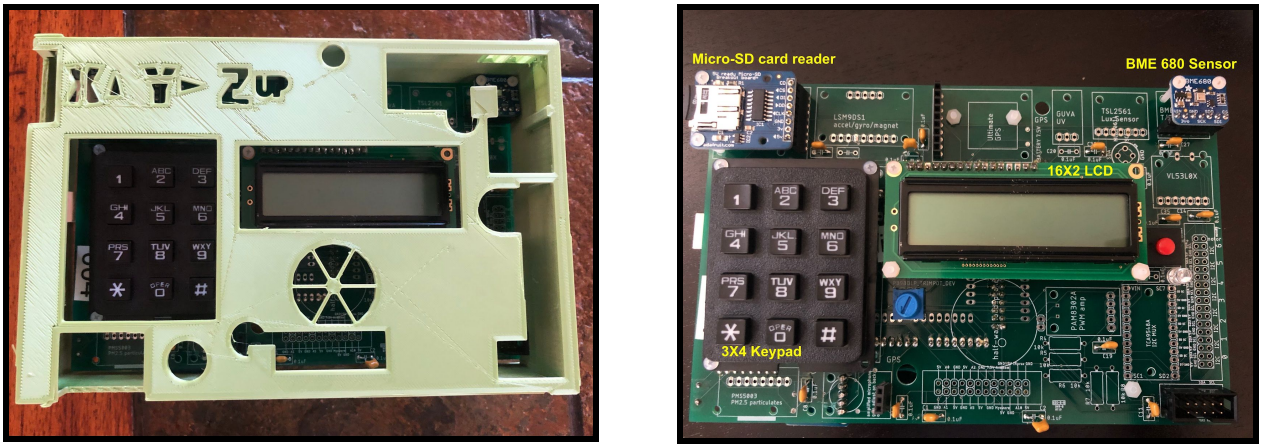

***Figure 15a**: PCB with 3D printed case (Left)*
Front: LCD, keypad, potentiometer, BME680, micro-SD, ribbon cable connector (Right)

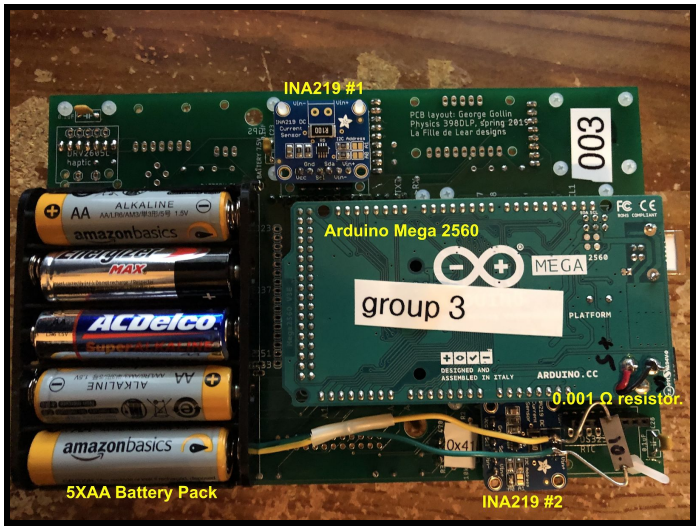

***Figure 15b**: PCB Back: 5AA Battery Pack, 2 INA219, Arduino Mega 2560*

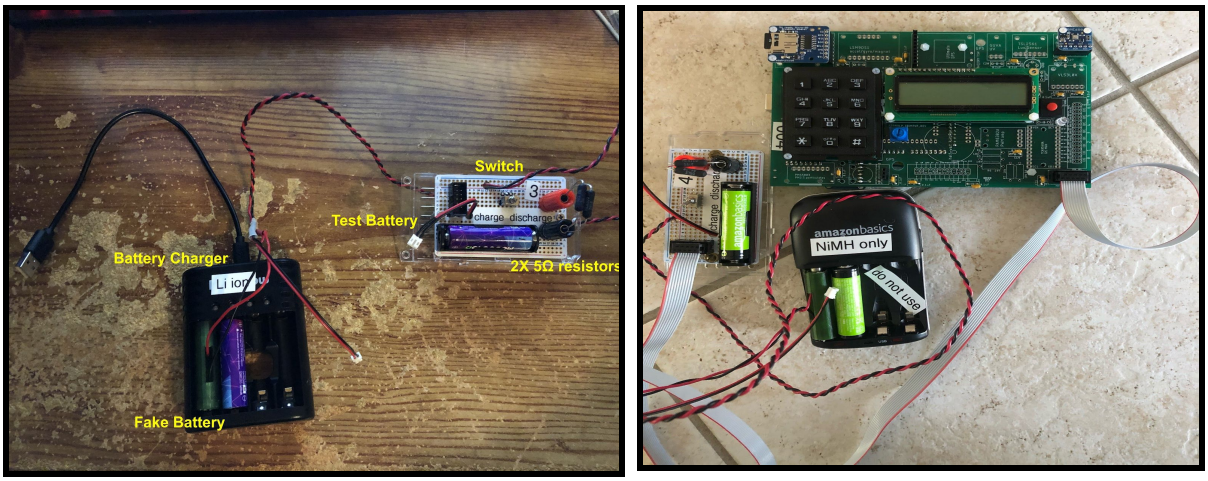

***Figure 15c**: Protoboard and fake battery (Left)*
PCB, protoboard, and charger complete experiment set up (Right)

2.3 Data Acquisition Software

The goal for the data acquisition (DAQ) was to record the current, voltage, and ambient temperature of the battery throughout tests. The DAQ was developed in C++ on the Arduino's integrated developer environment. The following gives an explanation of the program's design.

Beginning with the libraries that were utilized, the AdafruitKeypad.h library allowed for user input to be given via the 3X4 keypad, while the SD FAT library created text files and wrote data into them. The AdafruitSensor.h and Adafruit_BME680.h library enabled the BME680 to output the ambient temperature, atmospheric pressure, and humidity values detected. The AdafruitINA219.h library was used to produce measurements of current and load voltage. Finally, the LiquidCrystal.h library was used to write information onto the 16X2 LCD display. These libraries were used to complete the test procedure explained below.

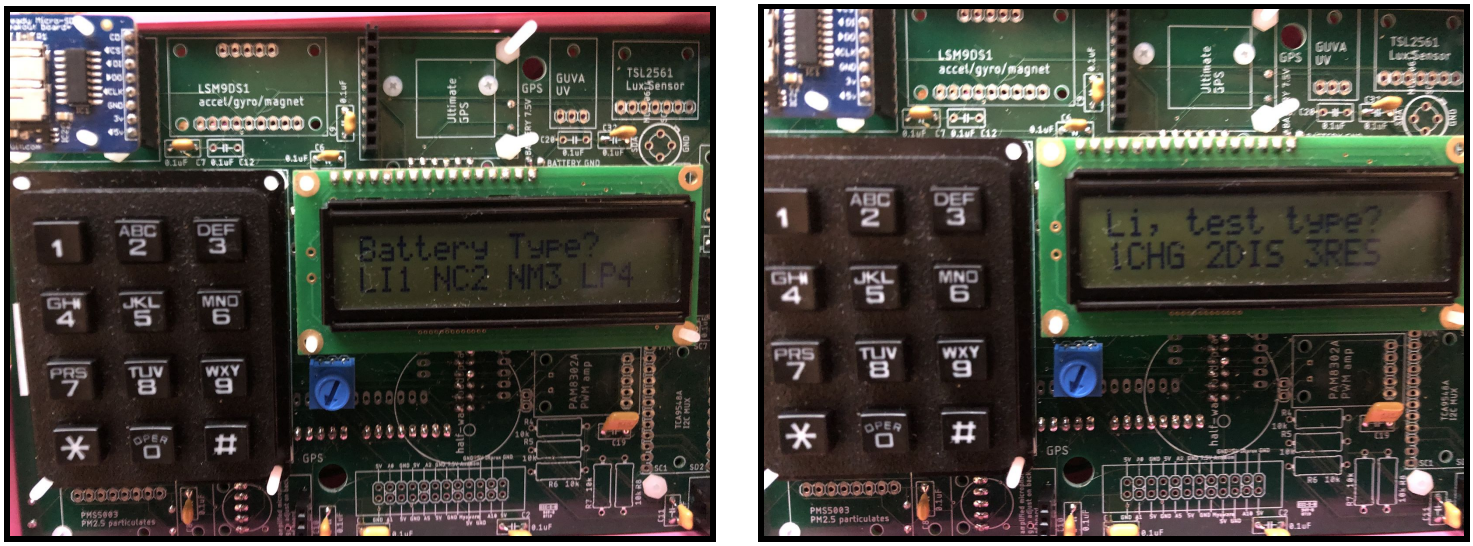

***Figure 16**: First menu when PCB turned on (Left)*
Second menu after first selection in first menu (Right)

First, the LCD prompts the user for the type of battery being tested. An input of keys 1-4 will cause the program to tag the text file with the corresponding battery type. After the system receives an input, a second menu prompts the type of testing data being generated: charging or discharging. The third option allows users to return to the battery menu to reselect the battery type. As seen in Figure 16, the menu can be interpreted relatively intuitively. The number next to the desired test battery type should be selected. Then, the LCD displays updates with the battery type selected and a menu for test selection. Three options are given: charge (1CHG), discharge

(2DIS), or reset (3RES). The reset function allows users to select a battery type again. Using the same logic, the desired test type can be selected.

When all the necessary information is received, the test begins. Data from both INA219's, the BME680, and millis() function on are outputted to the text file. The millis() function supplies the milliseconds since an Arduino is powered on. These measurements are repeated until the program is terminated by the keypad input "77" from the user. After it is terminated, the text file is closed and the amount of data points collected is displayed.

2.4 Test Procedure

After loading the DAQ onto the microcontroller, the following procedure is followed to produce text files which can be analyzed using python.

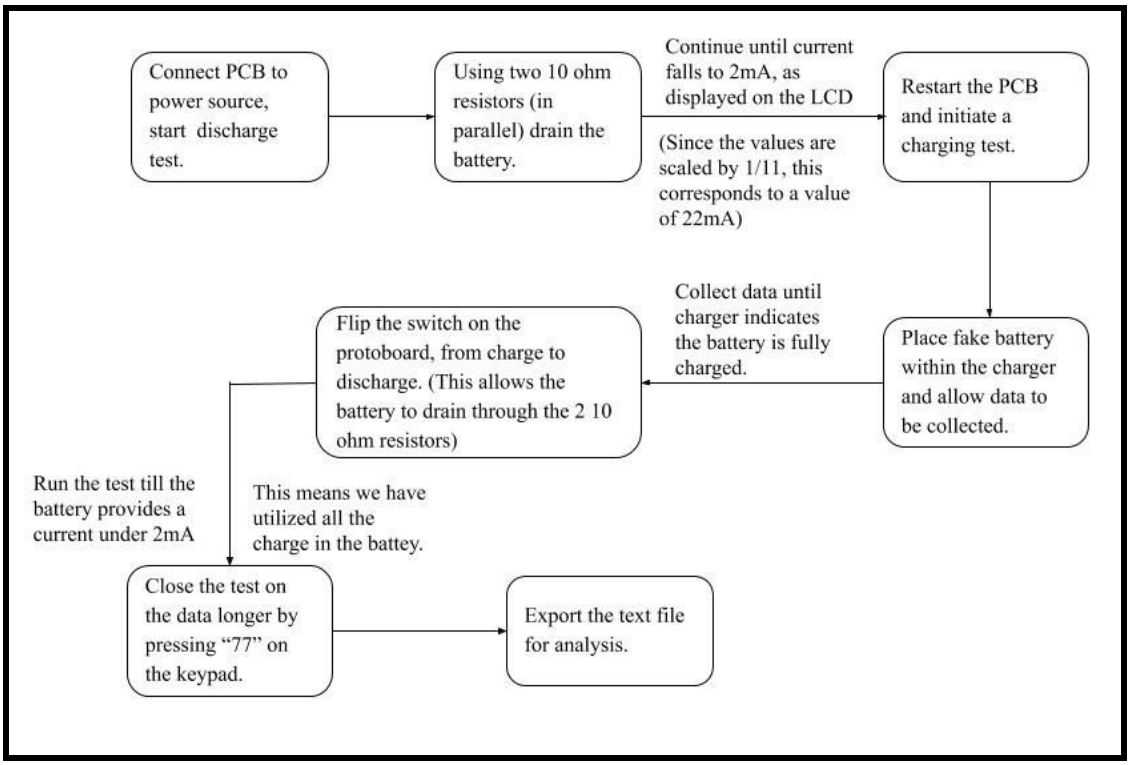

Diagram 1 *: Procedure for each battery tests*

The text files generated from this testing procedure are used to generate plots and ratios which are displayed in the following sections.

3 Analysis of Methodology

Now that a reliable testing procedure has been established, an analysis of its reliability must be performed. The main sources of error investigated are the noise in the INA219 measurements and the unreliability of our sample rate regarding the charger pulsing as discussed in Section 1.

3.1 Noise from INA219

To do an analysis of the noise seen within the INA219 measurements, discharge currents of a Ni-MH battery will be used. Since the Ni-MH battery does not have internal circuitry and the discharge current is continuous, the current will be stable enough to isolate noise from the INA219 while taking relevant measurements (Vassal, 1999).

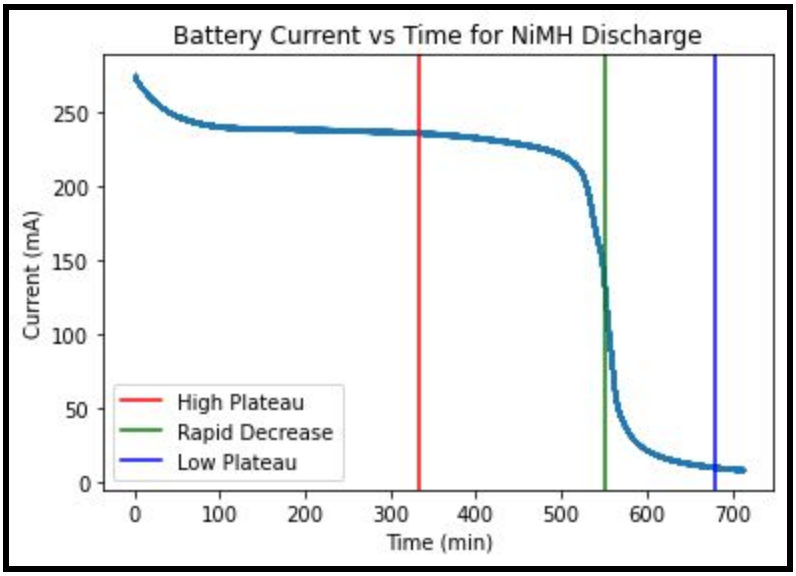

***Figure 17**: Plot of discharge current for a Ni-MH battery under 5ohms load at 25C°. Three regions of current values are established and correspond with sections to be analyzed.*

To see if the magnitude or slope of measurements affect the noise, the analysis considers 3 regions: High Plateau, Rapid Decrease, and Low Plateau. The three lines within Figure 17 demonstrate where data is being drawn from. The high plateau segment of the discharge data corresponds to the region in which the battery operates around the nominal voltage. The rapid decrease region corresponds with when the battery begins to lose voltage rapidly, corresponding to a significant current decrease. Finally, the low plateau region represents the current collection after the battery loses all of its effective energy. The plateau sections are dynamically determined

by scanning for the last nominal values and first low values which are acceptably linear. The rapid decrease region contains the midpoint between our nominal values and the 22 mA cutoff.

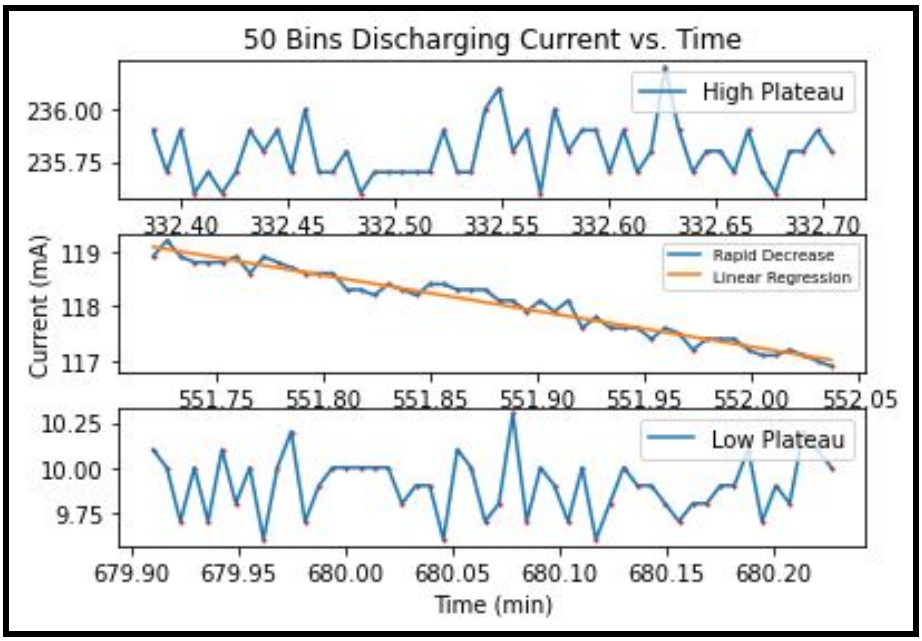

***Figure 18**: 50 bins of discharge data from each subsection as previously defined in Figure 17*

Figure 18 shows 50 bins from the three ranges indicated in Figure 17. There is little evidence of a periodic relationship in the graphs associated with the plateaus, as shown by upper and lower panes. However, when viewing a scatter of the rapid decrease against a linear regression, there is some slight evidence that a periodic relationship could exist. As a result, mathematical models will be used to break down the noise, allowing consideration of possible sources and their effects.

To investigate the existence of any periodic relationships between current and time, a Lomb-Scargle analysis was used. A periodogram, created using this analysis, is a well established equivalent to Fourier Transforms for unevenly sampled data. The purpose of Fourier Transforms is to break down a periodic signal into a collection of cosine and sine functions, which allows for a better understanding of the components in the periodic signal. As a result, the analysis was used to break down the measurement residuals, from a linear regression, into the constituent frequencies and amplitudes. Measurement residuals are the differences between observed and expected values from a statistical model. The periodogram can be used to examine the magnitude of the periodic signals within our data collection. However, to increase the accuracy of our test, 1000 bins of data was used as displayed below.

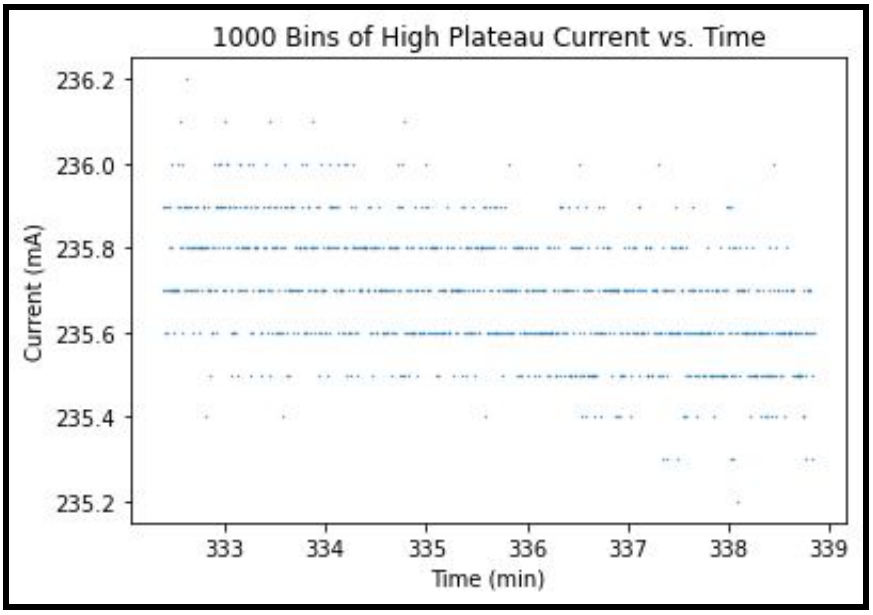

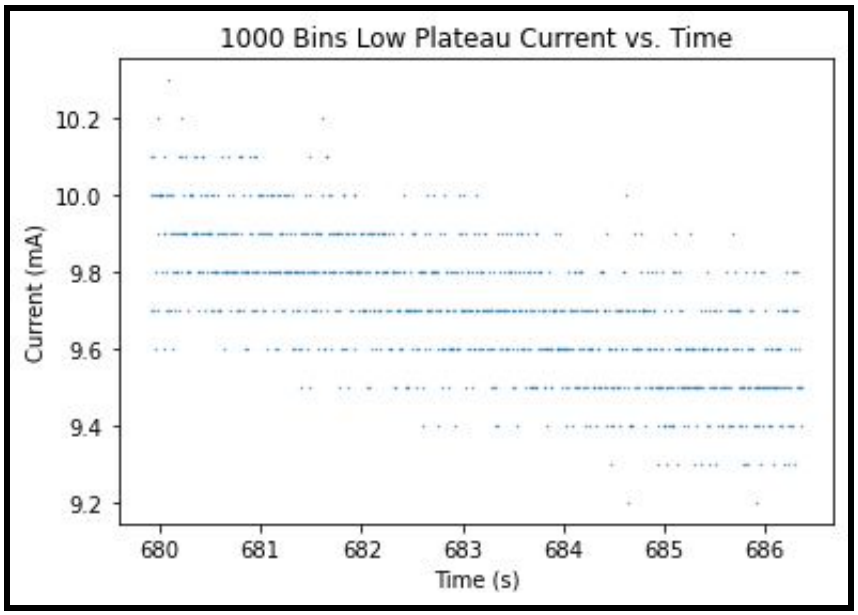

Figure 19*: Caption is below with the final graph in the figure.*

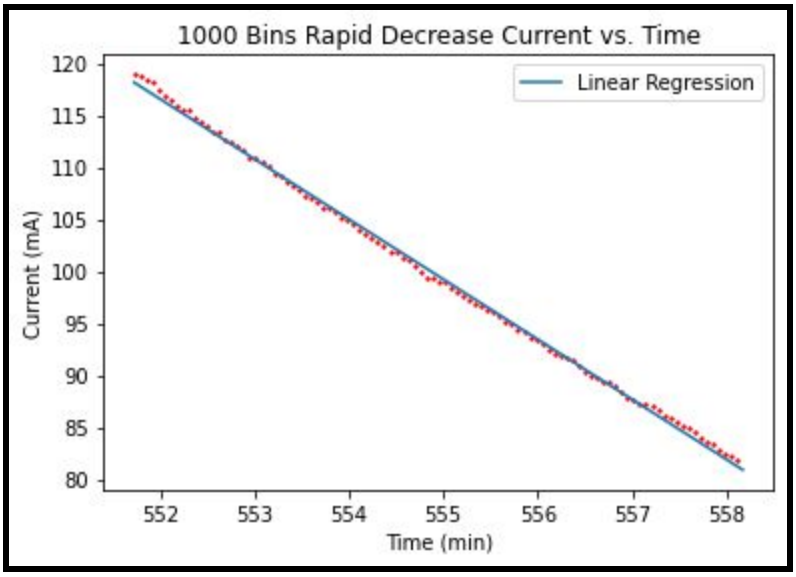

Figure 19*: 1000 bins of discharge data from each subsection of our discharge as previously defined in Figure 10. Note: For rapid decrease, only every tenth point is shown to allow the periodic relationship around the linear regression to be more evident.*

The graphs of plateaus within Figure 19 show definite evidence of a quantized measurement system and a small linear trend. With the quantization of the measurement system being so prevalent in these regions, the results from the Lomb-Scargle may not be as reflective of the actual signals. In general, the responses from the analysis would be of smaller magnitude compared to the actual signals. However, as the rapid decrease region spreads over a larger range, quantization has a less visible effect allowing for more reliable results. Similar to the 50 bin analysis of rapidly decreasing current, there is more evidence of an oscillation around the linear regression. For ease of viewing this oscillation, only every tenth data point is displayed. A cycle of the oscillation can be seen to start at minute 552 and end at minute 558. Considering this oscillates over the course of about 323 seconds, it is expected for a corresponding peak to appear in the Lomb-Scargle periodogram. To quantify these periodic signals, all regions are fed into a Lomb-Scargle analysis. Through this analysis, the functionality and resolution of the INA219 can be proven capable for this experiment.

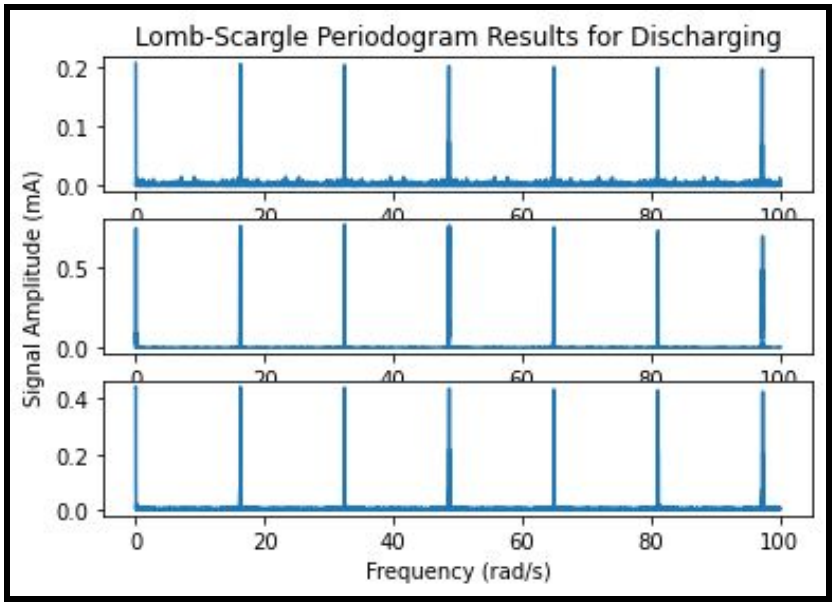

***Figure 20**: Lomb Scargle Periodogram graph for Ni-MH discharging data.*

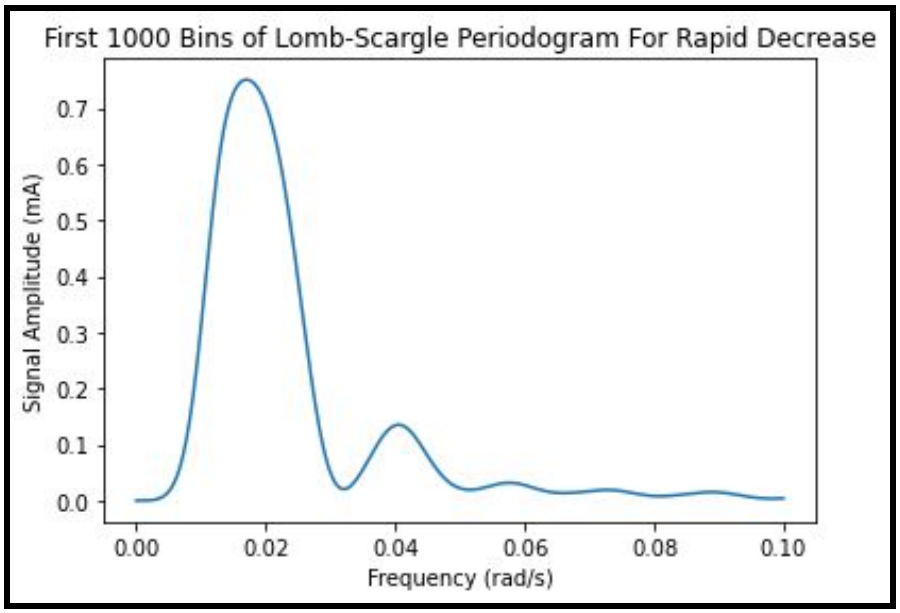

***Figure 21**: First 1000 Bins of Lomb-Scargle Periodogram graph for Ni-MH discharging data.*

The reliability of this analysis is proven by the peak at the frequency corresponding with the signal seen in Figure 19. With a time period of 323 seconds, a peak at a frequency of 0.019 radians per second was expected. The first 1000 bins within the results for Rapidly Decreasing current show a signal with magnitude 0.77 mA and frequency 0.018 radians per second.

Figure 20 can indicate conclusions about the effectiveness of the INA219. As all three regions show similar results, it can be inferred that the peaks are dependent on the measurement system's quantization and noise. As expected, the largest magnitude signals are seen in the rapid decrease results, followed by low plateau and high plateau. This is because a smaller range of values leads to the quantization diluting the results more. However, these signal magnitudes are still insignificant as they correspond with 0.5% of the discharging current and less than the INA219 quantization. Similarly, the frequency for the majority of spikes are very large, implying these signals undergo countless oscillations throughout the experiment. As a result, their presence will have little effect on measurements collected from the INA219. From this, it is concluded that the INA219 is capable of measuring current for this experiment.

3.2 Charger Cycles

An analysis of the chargers used must be performed to create an accurate evaluation of the amount of energy transferred during the charging cycle. Specific battery types require different types of processes to maximize charging efficiency and speed. However, since Ni-Cd and Ni-MH are chemically similar, they use similar processes that revolve around duty cycles. In circuitry, a duty cycle expresses the ratio of time a load or circuit is on, compared to off, over a time period. The goal of this section is to establish a better understanding of how the duty cycle should be factored into the power integration considering the fact that the measurement frequency is significantly less than that of our charger's cycle. This section does not apply to Li-ion as it is charged with constant current and close voltage monitoring.

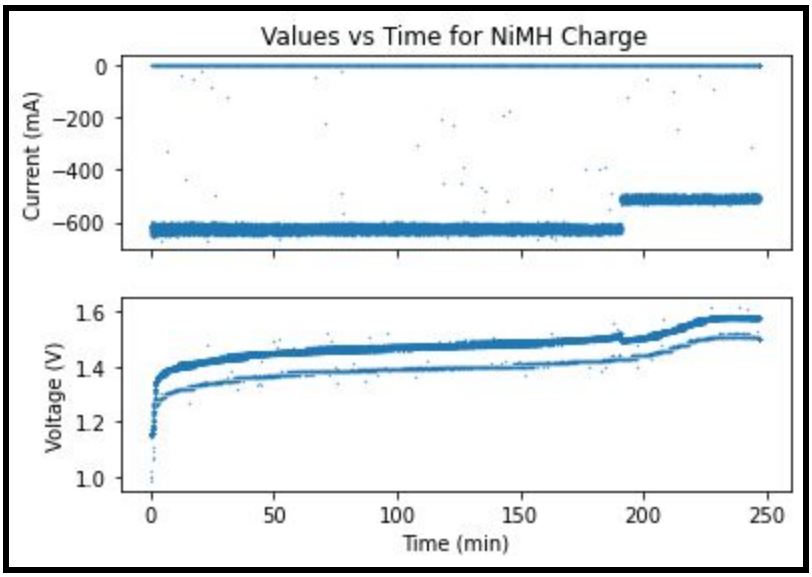

***Figure 22**: Current and Voltage for the charging of a Ni-MH battery at 25°C.*

Figure 22 is the result of charging a Ni-MH Battery. The graph of current in Figure 22 shows obvious signs of a duty cycle within the charger. Within the scatter plot, there are three consistent measurements, which give indications of two different charging cycles. The first segment which is located at 0 current corresponds to the off-time within the duty cycle. As to be expected, this exists for the entirety of the charging process. The other two segments, at -640 and -510 mA, correspond with the charging current supplied during the on state in the duty cycle. Further evidence of this is provided by the voltage graph. The existence of a bimodal response indicates a state change within the circuit which causes the battery to shift from one voltage to another. The upper line corresponds to voltage values recorded when the charging circuit was active, while the lower line represents the voltage when the charging circuit was inactive. Based on the following figures, it appears that the duty cycle is dynamically determined by the test battery voltage. By monitoring voltage values and changes during each cycle, it ensures that the battery is not overcharged or damaged.

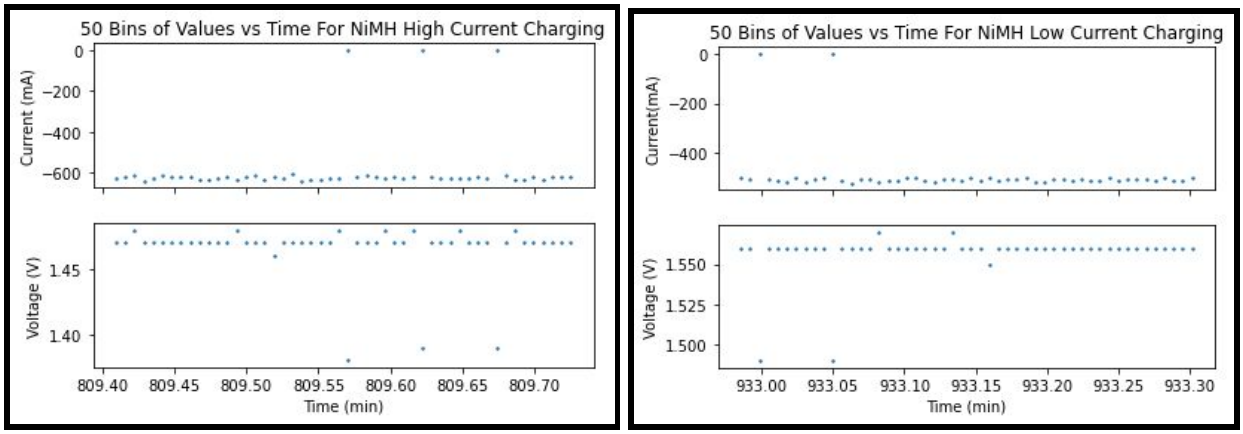

***Figure 23**: 50 bins of Current for charging a Ni-MH battery.*

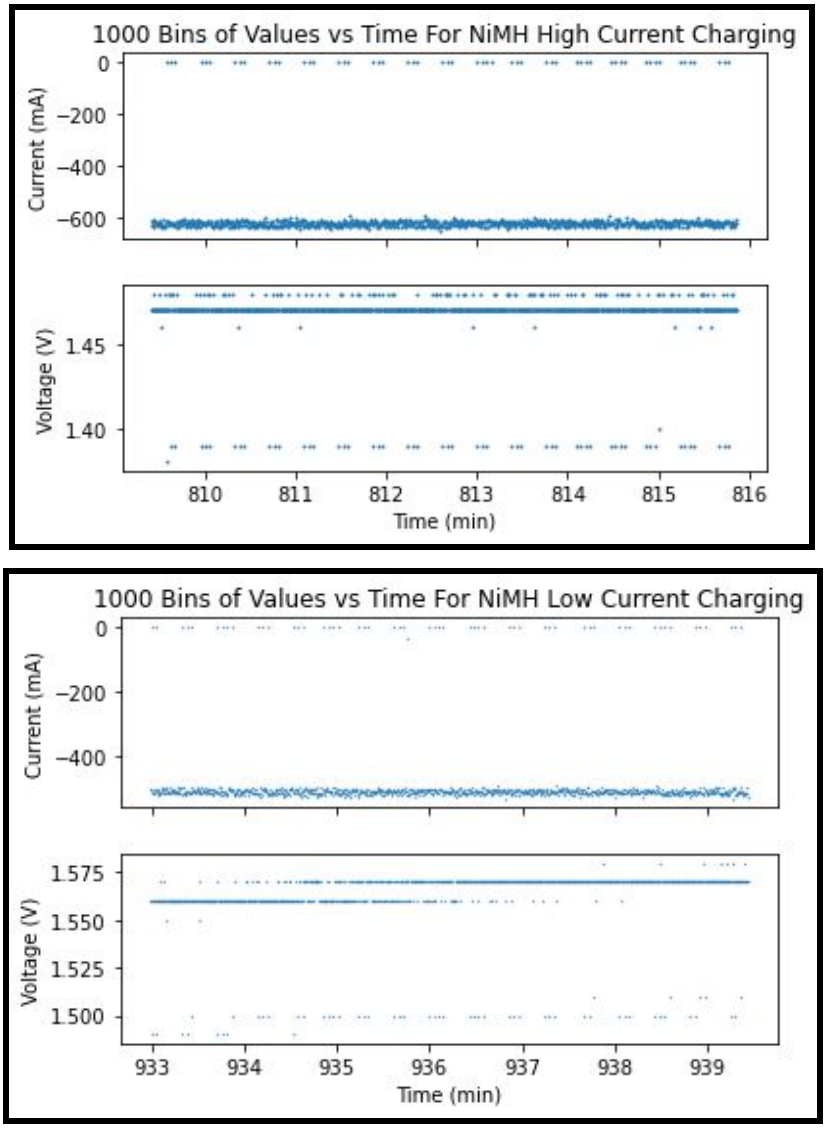

***Figure 24**: 1000 bins current for Ni-MH oscillation.*

Figures 23 and 24 show that the low voltage measurements correspond with 0 mA measurements. Due to the frequency at which the INA219 collects data, there is still little evidence of an exact ratio. Figure 24 shows a larger collection of data and clearer indications of a duty cycle occurring. As 0 mA measurements periodically align with when data is being measured, there is more evidence that a higher sampling rate must be used. To thoroughly understand these cycles, a shorter program was used to gather readings from the INA219 at a considerably larger frequency.

The resulting graphs exhibit the charging process more closely, since the new program takes a measurement every millisecond and stores them within the Arduino's memory. After 200 data points are collected, data collection ceases until all of these values are exported to the text

file, resulting in the periodic time slots with no measurements. Due to the limitations of the Arduino, enough data points to display an entire cycle cannot be maintained in memory. However, this method still provided adequate data to determine duty cycle percentages.

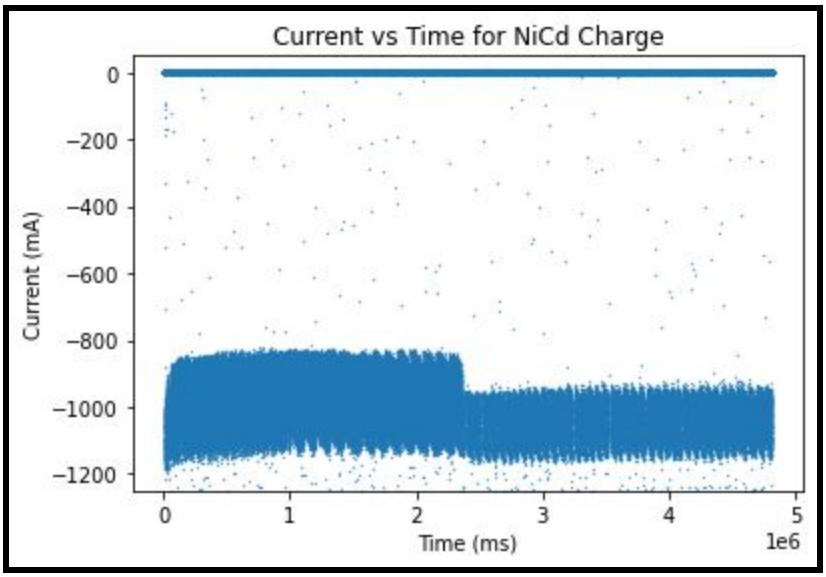

***Figure 25**: Ni-Cd charging cycles with close measurements.*

Figure 25 shows the charging process for a Ni-Cd battery. It should be noted that the current does not change within the Ni-Cd charging process, as occurred within the Ni-MH process shown in Section 3. The duty cycle changing can be seen to change around the $2.35*10^6$ ms mark. This is shown by the change in current bounds. It may be observed that the general shape of the scatters change at $1*10^6$ ms. However, these changes are not observed in individual cycles. Figure 26 displays the first duty cycle within the Ni-Cd charging process, while Figure 27 shows the second.

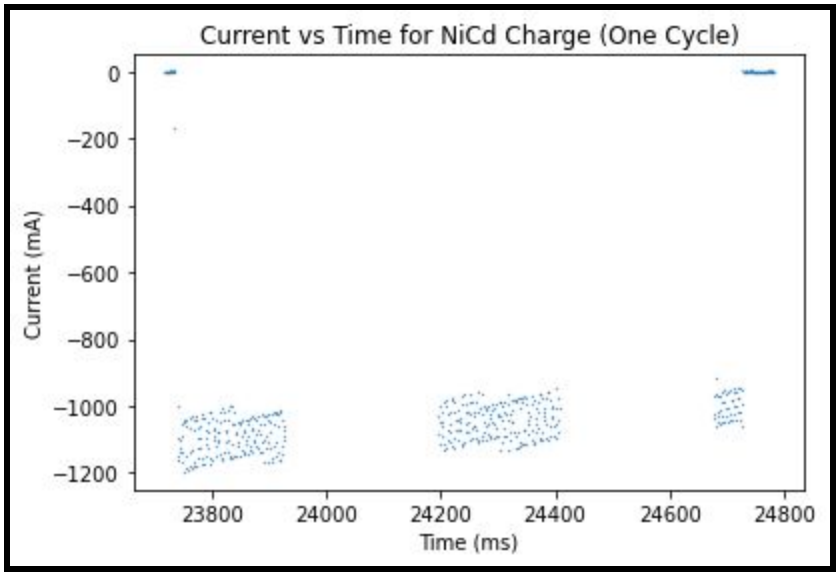

***Figure 26**: A single charging cycle in the beginning of the charging process.*

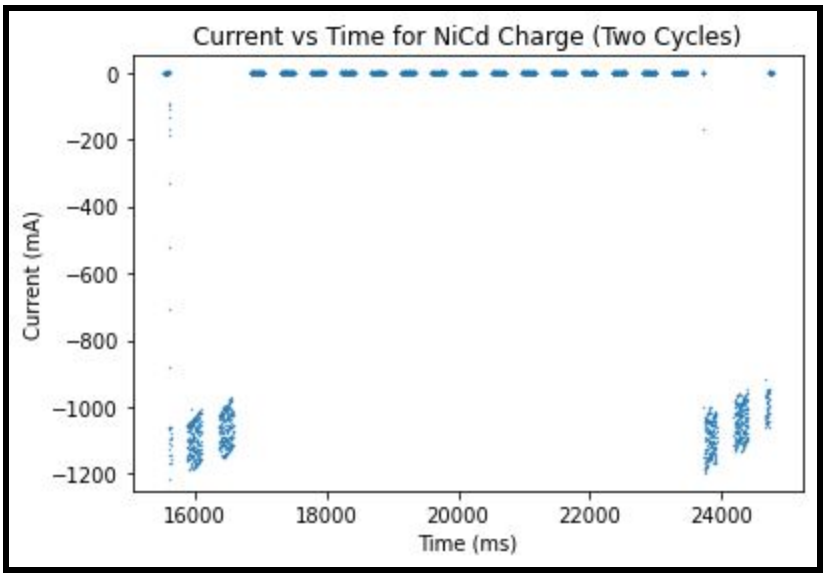

***Figure 27a**: Two charging cycles in the beginning of the charging process.*

The plot in Figure 27a shows a single cycle, illustrating evidence of a specific current range being maintained until the end of the on cycle is reached. The plot of Figure 27b shows the existence of periodic cycles, where the time period of one cycle is approximately 8132 milliseconds. Throughout this process, approximately 1123 milliseconds are spent with current being delivered, giving a duty cycle around 15%. Over the analysis of many cycles, this tends to be a good approximation until the shift that occurs at $2.35*10^6$ ms. At this point, acceptable current limitations of the step function shift to be slightly higher and the duty cycle decreases, shown by the following figures.

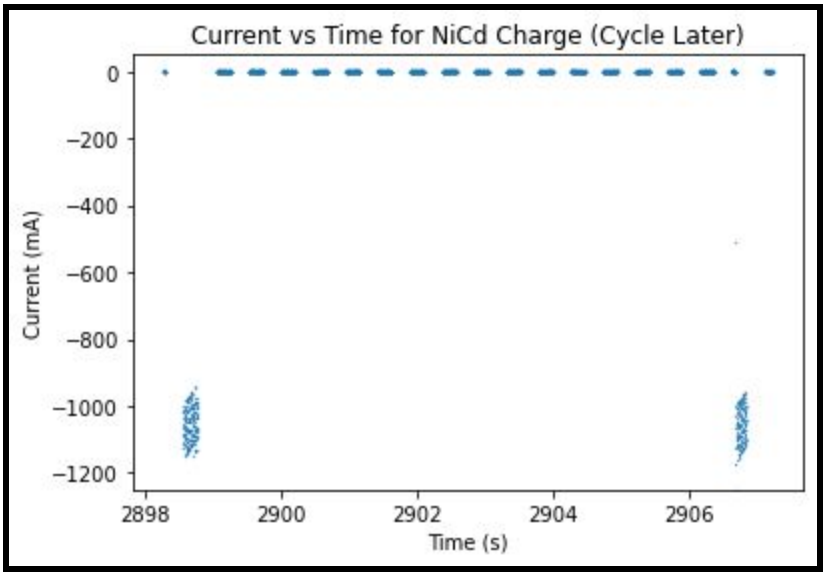

***Figure 27b**: Two cycles later in the charging Process*

Within this figure, the overall cycles of a similar frequency, but lower duty cycles. The peaks show the current is supplied for approximately 242 ms, giving a 3% duty cycle.

This analysis was performed for the Ni-MH chargers and led to a similar understanding of the duty cycle. Some of these graphs are shown below in figure 27c. As the frequency of these cycles were higher than Ni-Cd, displaying the results became more difficult. The duty cycles had to be observed over a few dozen cycles to create a matching step function. After finding this ratio and time period, the duty cycles were calculated using the same methods used previously. When analyzing the high current section, shown in Figure 22, the Ni-MH charger used a 80% duty cycle. However, in contrast to the Ni-Cd charger, the duty cycle increased later in the process as the supplied current was lowered. When the transition occurred, the duty cycle increased to 99%. It should be noted that this results in equal rates of power transfer. Having an understanding of what the INA219 measurements are displaying, less frequent measurements can be used to accurately calculate the energy transferred, while other measurements, such as temperature, are being provided.

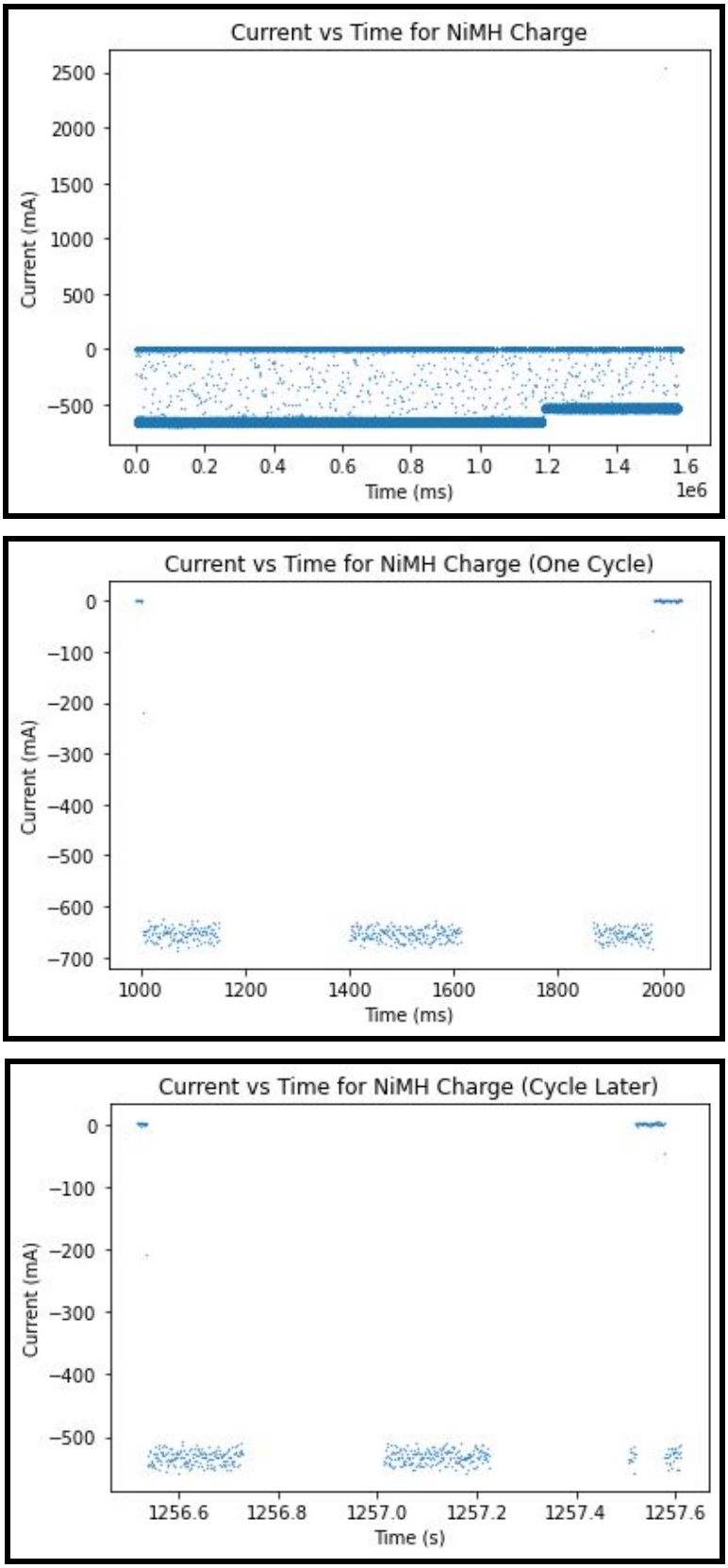

***Figure 27c**: Some graphics for the NiMH process.*

4 Results

As the methods of data collection have been thoroughly documented, the analysis of the resulting tests will be provided. A ratio of the energy emitted during the discharge process to the energy transferred during the charging process will be used as a measure of the efficiency of the batteries in different working conditions. The following plots show the relationship of current and voltage as a function of time for Li-Ion, Ni-Cd, and Ni-MH batteries at normal and cold temperatures.

4.1 Normal Conditions Analysis

The analysis begins with “normal” operating conditions. For these tests, the batteries were subjected to room temperature conditions, 25°C. In each case, the batteries were discharged through the same load, 5 Ω given by two 10 Ω resistors in parallel. The efficiency of different batteries is affected by the rate of discharge which could lead to a constant offset within the energy efficiency ratios calculated. These factors are not considered within our calculations.

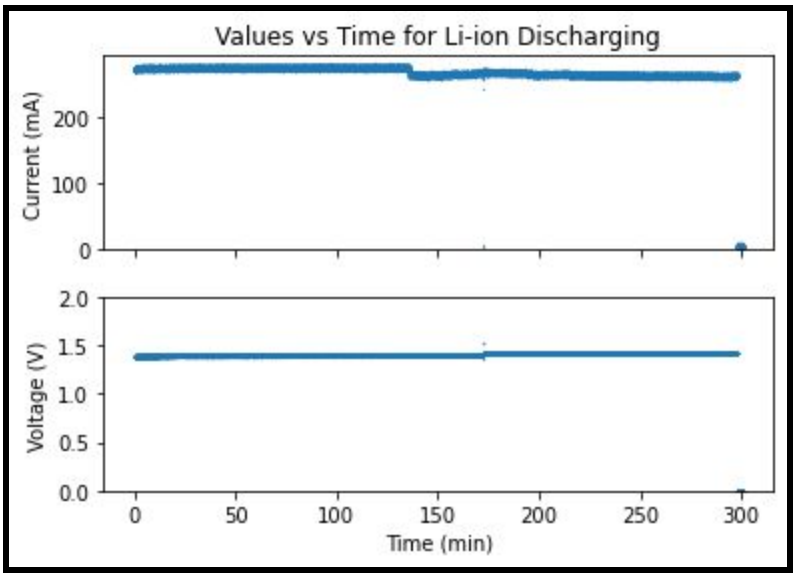

Figure 28*: Current vs time for Li-Ion for discharge state at room temperature. While the voltage seems to remain steady for most of the run time, the current fluctuates more than expected, indicating the effect of the internal regulator on the behavior of the battery.*

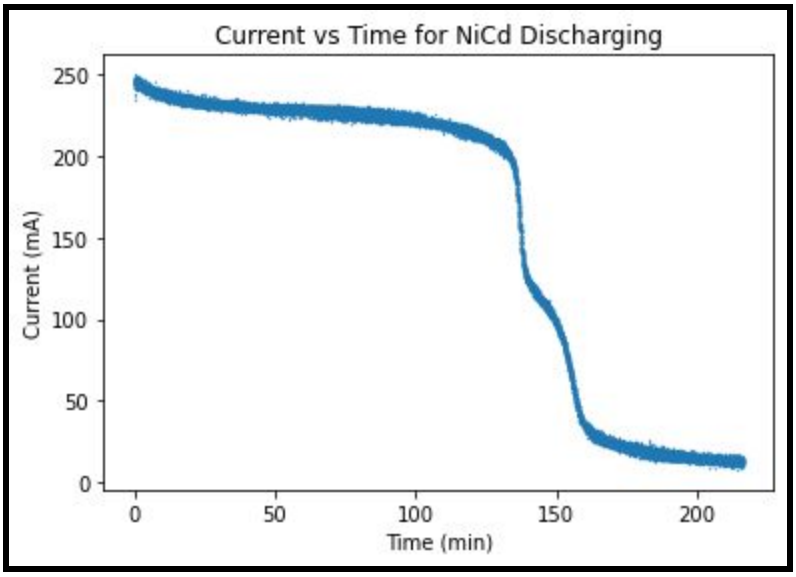

Figure 29*: Current vs time for Ni-Cd for discharge state at room temperature*

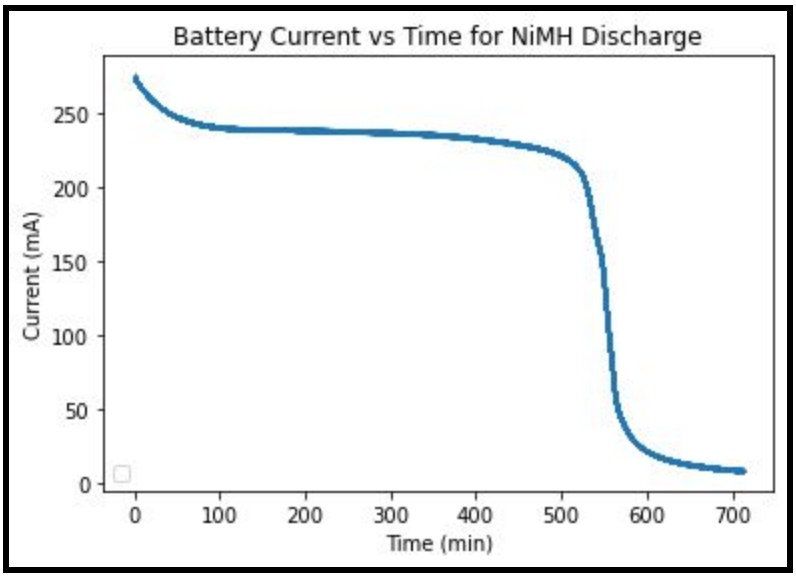

Figure 30: *Current vs time plot for Ni-MH for discharge state at room temperature*

In Figures 28, 29, and 30, the nickel-based batteries appear to follow a similar curve with slight differences depending on the capacity, while the Li-ion curve appears similar to a heaviside function. The curve of the nickel-based batteries shows a continuous current curve, which eventually decreases rapidly when the available energy is depleted. More evidence of overcharging is displayed by the higher current at the beginning of trials. In the case of the Li-ion battery, which has a voltage regulator, it can be seen that the voltage decreases to precisely 1.45 volts when a discharge begins. This is less than half of the nominal cell voltage, but within the regulations of a AA battery. This voltage is maintained until the battery is unable to supply

enough power to maintain this voltage through the regulator. At the 297 minute mark, the current and voltage immediately drop to 0 indicating the regulator is not able to maintain the specified voltage and turns off. Approximately two hours into the Li-ion test, a slight drop in current values is recorded. This fluctuation is attributed to the internal regulator leading to an increased internal resistance within the battery. As voltage remains constant, this remains the only variable. This was observed in each test run.

For each battery, the amount of current supplied for the specified time corresponds with the capacity estimation given by the supplier. For example, in Figure 30, the Ni-MH took approximately 520 minutes to begin losing voltage, and therefore current, rapidly. This data would correspond with 8.66 hours of 240 mA current, or 2080 mAh which is very close to the approximate 2000 mAh capacity given by the supplier. Each value can be seen to correspond with the capacity estimates provided by the manufacturers and covered in Figure 2. Integrating the power from these discharge curves, an understanding of how much usable energy a battery contains after being completely charged is gathered. However, for this to be useful, a similar understanding of the charging data must be developed.

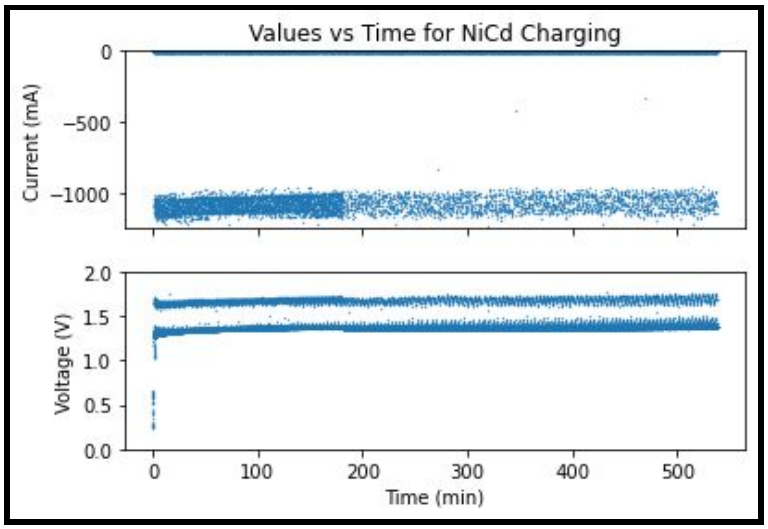

Figure 31 *: Voltage and Current relationship for charging cycles of Ni-Cd at room temperature.*

Figure 31 displays an entire Ni-Cd battery charging cycle which shows behaviors previously explored in Section 3.2. The bimodal segmenting of the voltage is the result of a charging duty cycle, as discussed previously. In the case of the Ni-Cd charger, the manufacturer has two different percentage cycles. Approximately 3 hours into this charging cycle, the charger switches from a 15% duty cycle to a 3% duty cycle. The duty cycle changes when a specific internal resistance value, and the corresponding battery temperature, has been reached. The difference in the percentage duty cycles can be seen by the density of the scatter plot decreasing after the 3 hour mark. The values within this plot shows that this battery charges at a significant

current compared to other batteries, especially compared to its capacity. In general, Ni-Cd batteries tend to charge at rates between 0.1-0.5 C, but in extreme cases can even approach 1C without seeing lasting effects on a battery's capacity. However, there are conflicting results as our smartcharger used a current of approximately 2C. Since the charger operates with a duty cycle, charging at high currents is possible. As stated previously, Ni-Cd batteries charge more efficiently at higher currents, but are not capable of maintaining these currents for long periods of time. As a result, the charger pulses high current at low duty cycles that allow for a trickle charge of 0.125 C, but at a current of 2C. While studying our data, the periodic measurements resulted in a similar density of expected measurements, even with larger spaced sampling. As a result, duty cycle was not required to be factored into integrating the power transferred.

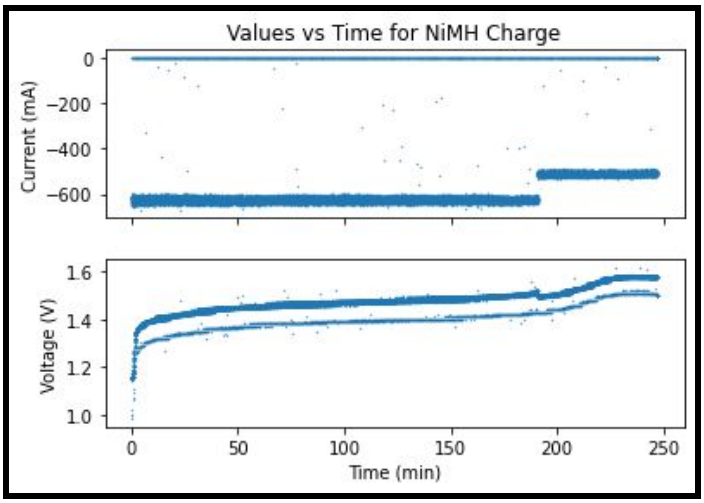

Figure 32 *: Voltage and Current relationship for charging cycles of Ni-MH at room temperature.*

Figure 32 shows the charging cycle for the Ni-MH battery. This cycle has been previously shown and discussed during section 3.2. However, the ability to make comparisons between Ni-MH charging and other battery types shows the importance of charging cycles. With nearly three times the capacity, but half the charging current, Ni-MH batteries charge in half the time of Ni-Cd batteries. Such a difference can be explained by the significantly higher duty cycle used within this charger. The fact that the charger runs at a 80% duty cycle for the first charging portion and 99% for the second translates into a charging rate of .25 C for the Ni-MH, despite the current being about .35 C. This behavior allows for a more effective charging of Ni-MH batteries which typically charge better under steady conditions. As was found in the previous data, the duty cycles were well represented within the collected data as the ratio of zero measurements matched the duty cycle percentages. As a result, there were no required alterations to the raw data collected when calculating the integration of power from the charger.

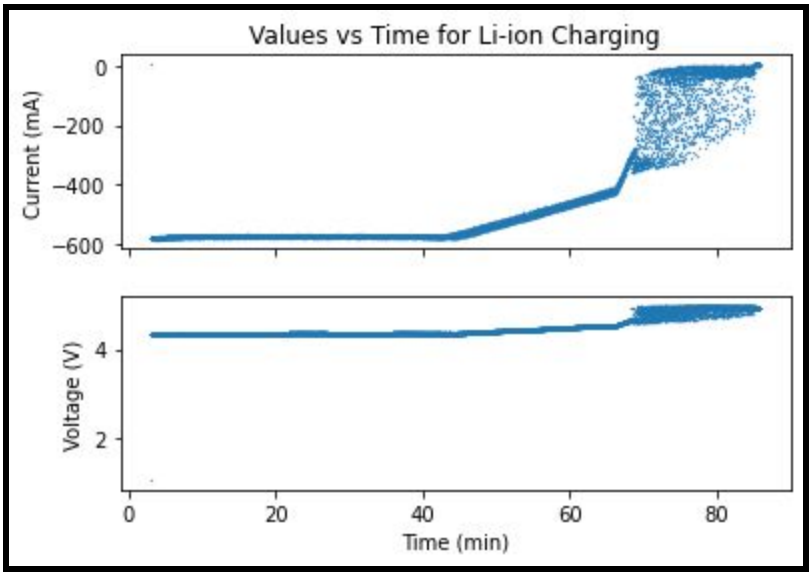

Figure 33 *: Voltage and Current relationship for charging cycles of Li-ion at room temperature.*

Figure 33 depicts the results from a charging test on a Li-ion battery. This data is not necessarily consistent with previous plots but is relatively simple to understand. Li-ion chargers work on a constant, dynamic feedback loop, attempting to maintain nominal cell voltage. The charging process is broken down into three sections: constant current, saturation current, and topping current. During the constant current region, voltage rises linearly at very small rates. When voltage peaks, a new current called saturation current continues charging the battery. However, saturation current decreases overtime. In most chargers, this decrease is exponential, but here a linear trend is observed from minute 40 to 65. After another peak in voltage, the topping current begins. This process closely monitors voltage and supplies currents in accordance until a steady nominal voltage of 4.2 volts is reached. As a result, current is maximized while voltage is maintained allowing for less lithium plating to develop on the anode. However, this feedback loop does not actually function off voltage in most cases. Most chargers function off of internal resistance values, which will be proven problematic.

In order to measure battery efficiency for each battery, input and output energy ratios were generated from current and voltage collected from the INA219. These were integrated, through a Riemann sum procedure, over the course of the entire charge and discharge cycle. The results of these integrations are shown below.

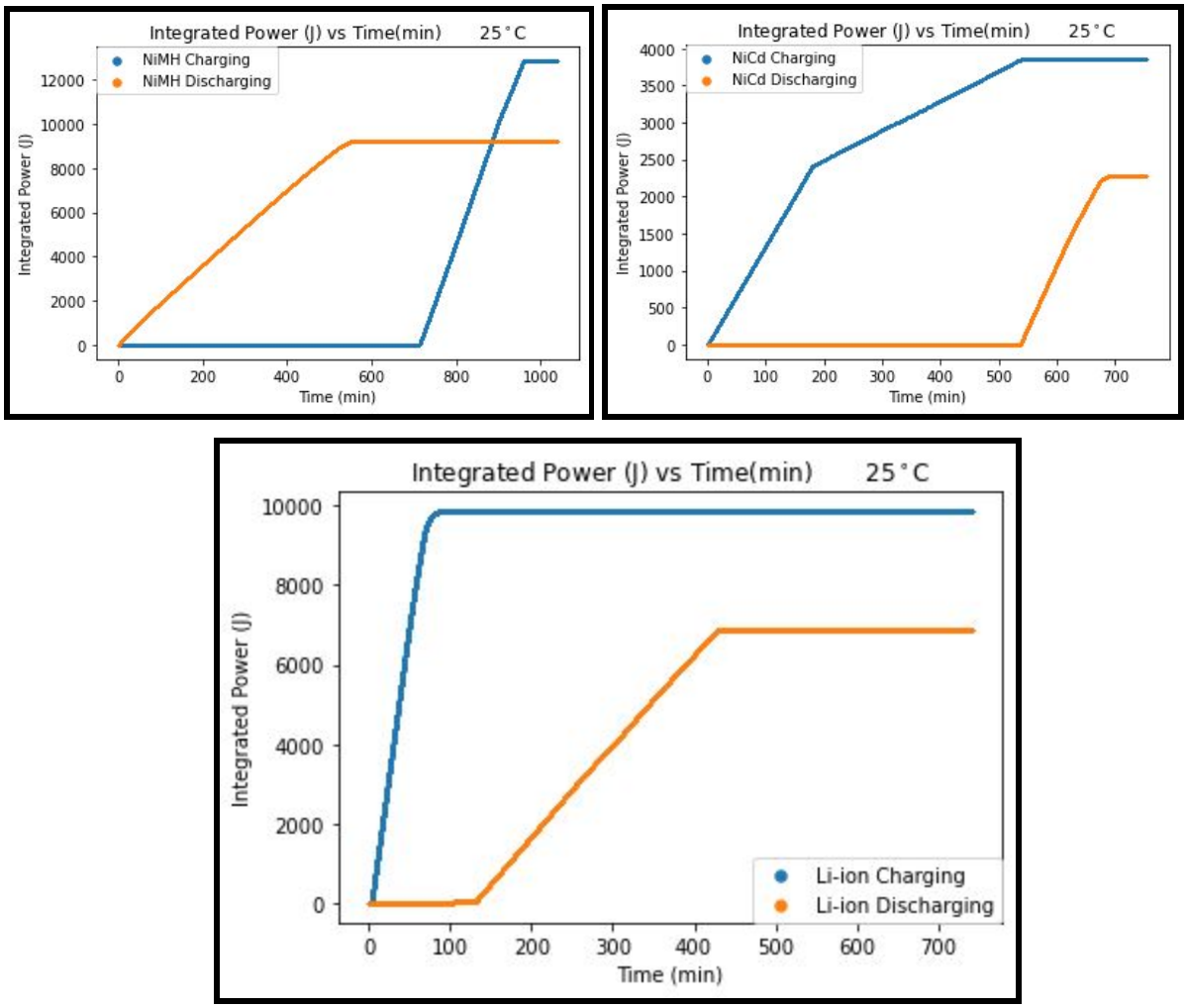

***Figure 34**: Power vs. time plots for Ni-MH, Ni-Cd, and Li-Ion at room temperature*

The integrated power for each battery test will be of a different magnitude due to the differing capacities of each battery; however, the ratio of the system's input energy versus output energy can consequently show the energy lost throughout the process of energy storage and data collection. Within each of these plots, the blue curve represents the integration of power during the charging process, while the yellow shows the results from discharging. These plots emphasize previously established relationships, such as the change of duty cycle in the Ni-Cd charging causing a change in the slope. Similarly, the Ni-MH slope remains constant throughout the entire charging process, establishing the constant rate of power transfer discovered in Section 3.2. Finally, a very steep charging rate for the Li-ion battery, which charged at around 1 C, is observed. However, the important relationship is the ending magnitude of the curves. Over the course of many tests, these calculations were performed to generate ratios of the magnitudes. These room temperature ratios, when averaged, led to general ratios of 59%, 72%, and 70% for Ni-Cd, Ni-MH, and Li-ion respectively.

4.2 Effects of Temperature

To examine the battery's energy input and output at different operating temperatures, tests were conducted at two different ambient temperatures. Battery tests were conducted under room temperature of 25 °C as a control. Other tests occurred at 5 °C to investigate the effects of cold temperatures in battery energy outputs and inputs. While trying to test higher temperature conditions, the testing equipment was proven to be unreliable. As resistance plays a large role within the circuit, the increased temperature resulted in similar charger errors. As a result, higher temperature tests were not successful and not included.

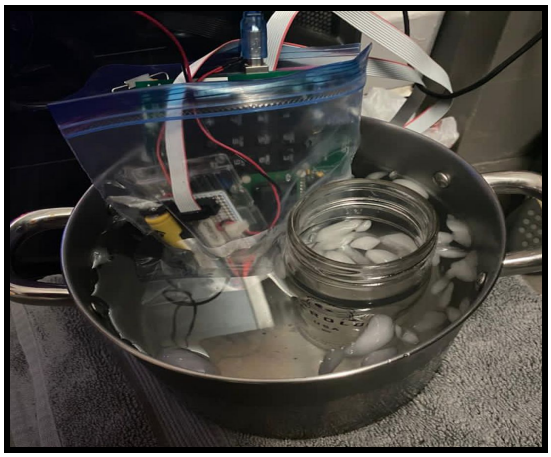

Figure 35*: Picture of the colder temperature setup. The PCB setup, which was connected to the data acquisition program, was placed in an ice bucket bath that measured around 5 °C.*

To conduct tests at lower temperatures, the PCB and breadboard were placed in an ice bath as shown in Figure 35 for both charging and discharging states. It is important to note that the INA219 collecting the current values is not submerged and able to calculate values without complications from the cold environment. The BME680 is approximately adjacent to the battery, which allows for accurate temperature readings. Overall, the ice bath battery tests follow the same procedures set in section 2.2.

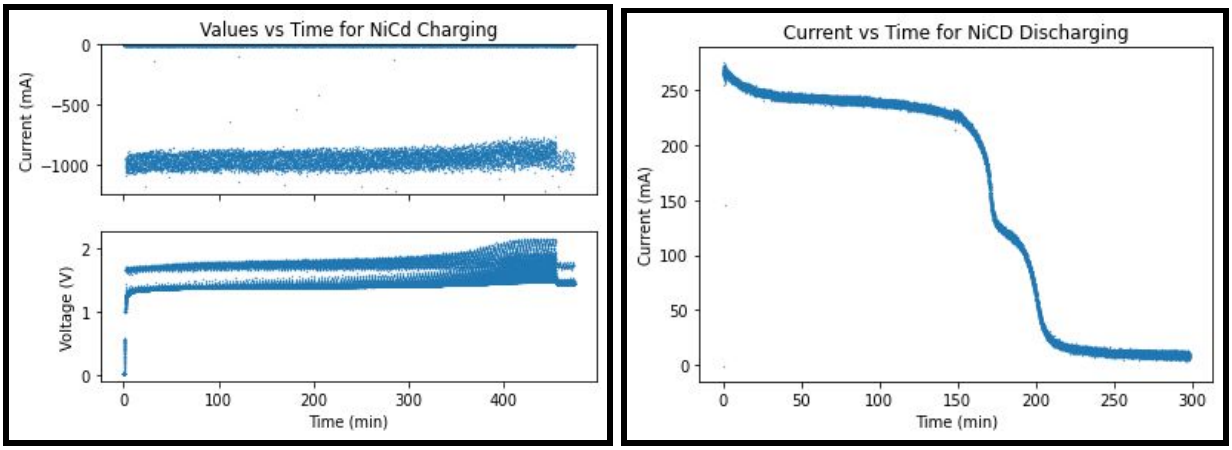

***Figure 36a**: Current and Voltage plots for Ni-Cd charging and discharging at 5 °C.*

When charging Ni-Cd batteries in lower temperatures, relatively little change in performance is expected. As mentioned previously in section 1, Ni-Cd batteries are the hallmark for maintaining functionality within cooler conditions. The charging curve shows slight differences, as the process takes less time and the switch between duty cycles occurs later. Both of these are expected because lower temperatures lead to the internal resistance of the Ni-Cd battery appearing lower, resulting in the duty cycle switch occurring later. As a result of the increased time within the first duty cycle, the time required decreases but the internals of the battery are likely affected. This is confirmed in the voltage peaking that occurs at values greater than 0.5 V above the nominal values at room temperature.

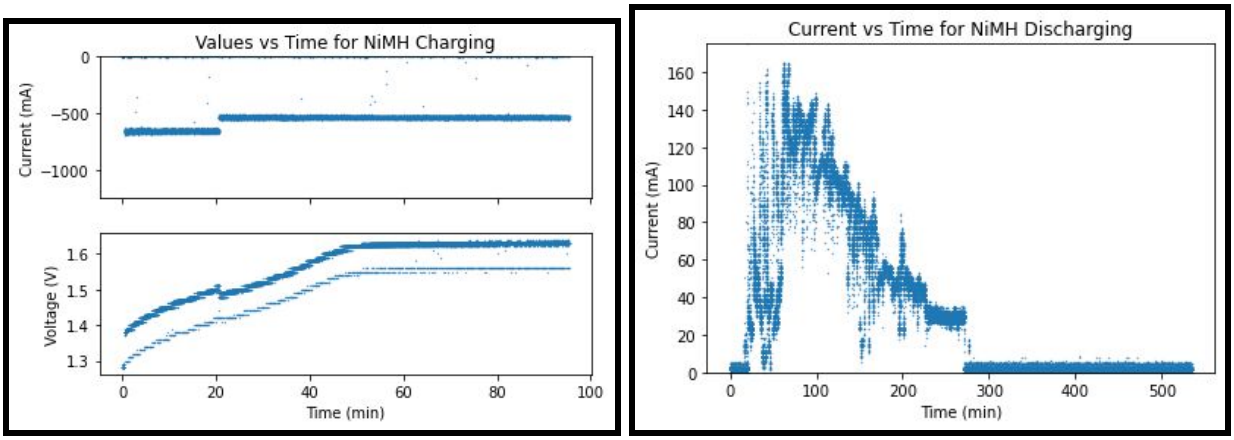

***Figure 36b**: Current and Voltage plots for charging and discharging at 5 °C.*

Figure 36b shows the results of testing a Ni-MH battery at low temperatures. As seen within Figure 2, the supposed working ranges of Ni-MH should include 5 °C. However, drastic changes are observed. The charging process follows a similar layout, but undergoes the cycle change significantly earlier within the process due to the voltage peaking quickly. However, in

the second duty cycle, a similar timeframe to the control is observed. The overall charging time is decreased by around 40%, leading to significantly less energy transfer. The process of discharging shows similar issues as steady currents are never obtained. Within this plot, little reasoning behind the erratic behavior can be found. The overall trend shows no signs of patterns. To better understand the improper functioning of a Ni-MH battery at this temperature, a method of collecting internal temperature and pressure may prove useful.

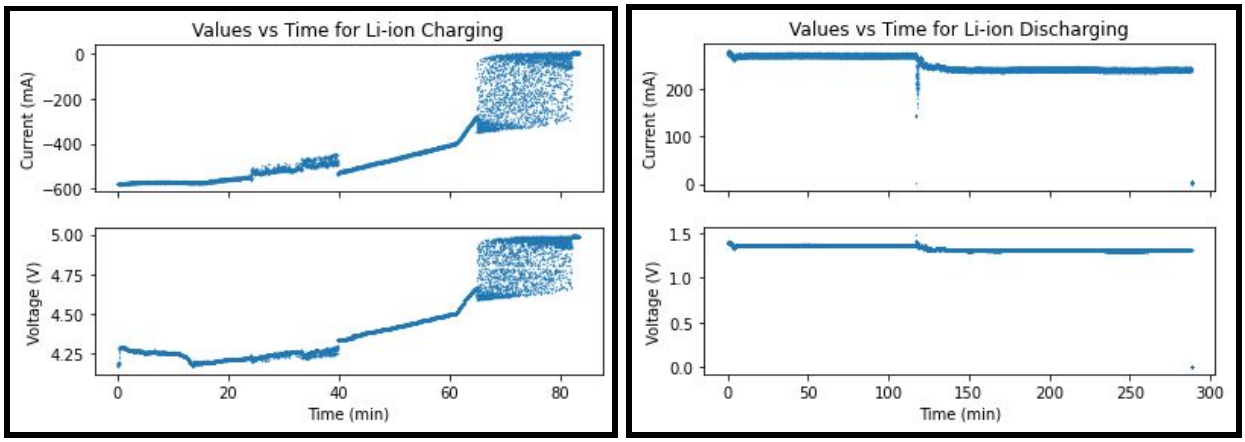

***Figure 36c**: Current and Voltage plots for charging and discharging at 5 °C.*

Figure 36c demonstrates the data collected for a Li-ion battery charging and discharging at 5 °C. As expected, the charging process proved dangerous since charging batteries below or around 0°C is typically not recommended. Even though it is possible, as indicated by Figure 2, charging at these temperatures leads to voltage peaking which causes lithium plating to form on the anode (Battery University, 2018), which may lead to the development of dendrites that cause battery failure. Within the charging plot, the faults of the charger, as mentioned previously, come to a head. The charger does not utilize voltage measurements as a means of determining the cycle switches, and as a result, the battery is overcharged. When in a lower temperature environment, the internal resistance of the battery is lowered. As this is the primary measurement used to determine the timing within the cycle, the battery is overcharged. The voltage curve mirrors the current measurements for similar reasons as seen in Section 3.2, as the amount of current flowing through the battery affects the voltage. Regardless of the irreparable damage caused by the charging process, we see similar performance while discharging at lower temperatures. However, the effects of the regulator seen in Figure 28, are amplified significantly. The voltage drop is nearly 4 times higher than seen within Figure 28, showing the significant effects of temperature on the regulator. Other than that, the discharge processes differ by minutes and maintain similar currents.

The energy ratios for batteries in cooler conditions decrease when compared to room temperature ratios. Differences in the power ratios can be attributed to the different charging cycles and chemical inefficiencies.

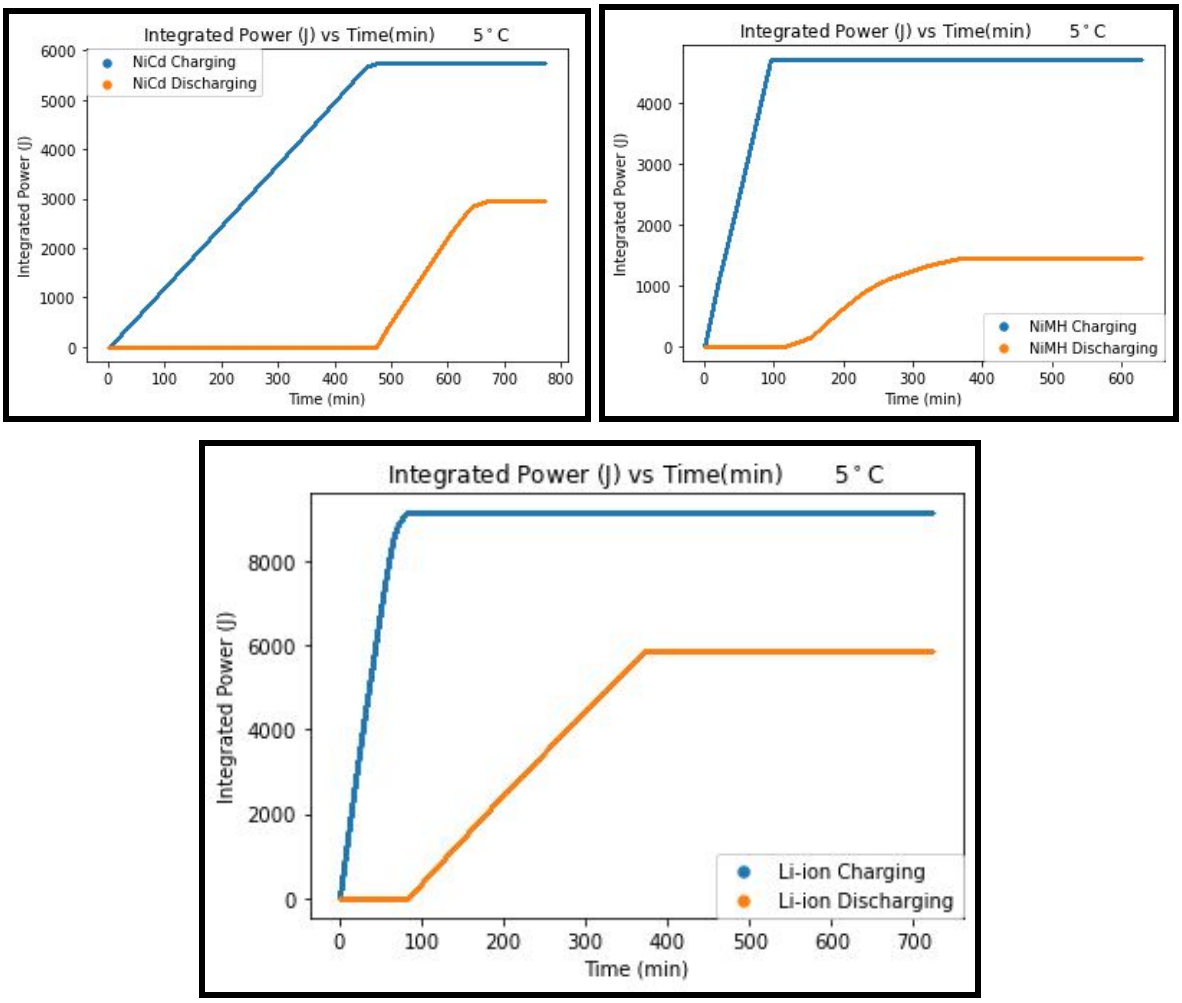

***Figure 37**: Integrated power vs. time plots for Ni-Cd at 5 °C.*

Figure 37 displays the integrated power vs time plots for the three batteries at colder temperatures of 5°C. The amount of energy transferred into a Ni-Cd battery at 5 °C is significantly larger than that at 25 °C. In general, over 2000 more joules are transferred over in this process, which consequently resulted in less than 600 J of usable energy. The Ni-MH power curve shows that significantly less energy was transferred and available for usage. For Li-ion, there is relatively little effect on the charging process and also output energy. This behavior is expected considering Li-ion batteries tend to lose only 10% of their capacity in cold temperatures. After averaging the results of many tests, Ni-Cd, Ni-MH, and Li-ion ratios averaged at 52%, 31%, and 64% respectively.

Conclusion

All three batteries, Li-Ion, Ni-Cd, and Ni-MH, showed the expected discharge cycle behavior at a room temperature of 25 °C. The Li-Ion battery, which was known to have a nominal cell voltage of 4 volts, met the AA criteria by utilizing a voltage regulator. Both the Ni-Cd and Ni-MH charging cycles showed the application of duty cycles described by the POWEROWL and AmazonBasics chargers. The reasoning behind duty cycles can range from preventing overcharging and damaging of battery cells to increasing energy and time efficiency. The charging behavior for Li-Ion batteries showed no evidence of duty cycles, but considerable evidence of a feedback loop that used measurements of characteristics to dynamically update the charging process. The results of the tests are summarized in the table below.

Battery Type	Cold (5 °C)	Room Temperature (25 °C)
Ni-Cd	0.5167	0.5933
Ni-MH	0.3074	0.7194
Li-ion	0.6424	0.6998

***Table 6**: Battery energy input and output ratios based on the integrated power calculations.*

After examining the computed ratios shown in Table 6, there are definite negative energy efficiency trends associated with the decreasing of temperature. The capacity and amount of energy needed to achieve full capacity depended on the chemical composition of each battery. However, decreasing temperature gave strong evidence to the energy efficiency of the batteries being negatively correlated with low temperatures. Further investigation of this conclusion will require data collection at various temperatures and output currents, as well as a statistical analysis of the various data collected to provide an understanding of the variance and confidence intervals of our results.

When conducting charging tests, there were technical problems in obtaining accurate and precise charging data. Complications arose from the battery chargers as they began to detect the resistance from the INA219. More problems arose when the Li-Ion charger output more than 3200 mA to charge, which was outside the unmodified INA219 range. The soldering of a precision resistor onto the INA219 provided the ability to collect data, but at significant costs. Approximately 3% error can be attributed to nearly every measurement. As our values have very linear trends, this error could be very substantial.

Precision resistors have low tolerance, meaning that there is less likelihood that the resistance will vary while in various conditions. To ensure the current readings being received were accurate, the precision resistors were required. For many batteries, there were still complications with certain batteries of a type not charging, which may be due to each battery's own internal resistance. To improve on charging battery tests, using a lower resistance current sensor with a higher resolution for our measurement range may improve on the data collected and analysis provided.

References

Abdin.Z, Khalilpour K.R (2019). Chapter 4 - Single and Polystorage Technologies for Renewable-Based Hybrid Energy Systems. *Polygeneration with Polystorage for Chemical and Energy Hubs,* 77-131. https://www.sciencedirect.com/science/article/pii/B9780128133064000045

B. Hariprakash, A.K Shukla, S. Venugopalan. *Secondary Batteries - Nickel Systems. Nickel-Metal Hydride: Overview.* Encyclopedia of Electrochemical power sources, December 2009. Retrieved from https://doi.org/10.1016/B978-044452745-5.00158-1

Battery University (2019, July 30). *BU-304:Why are Protection Circuits Needed?*. Battery University. https://batteryuniversity.com/index.php/learn/article/safety_circuits_for_modern_batteries

Battery University (2019, November 21). *BU-407: Charging Nickel-cadmium*. Battery University. https://batteryuniversity.com/learn/article/charging_nickel_based_batteries

Battery University (2018, April 24). *BU-409: Charging Lithium-ion*. Battery University. https://batteryuniversity.com/learn/article/charging_lithium_ion_batteries

Battery University (2017, May 9). *BU-303: Confusion with Voltages*. Battery University. https://batteryuniversity.com/learn/article/confusion_with_voltages

Battery University (2017, September 15). *BU-410: Charging at High and Low Temperatures*.

Battery University. https://batteryuniversity.com/learn/article/charging_at_High_and_low_temperatures

Berthold. E (2019, October 4). *Lithium-ion batteries*. Australian Academy of Science. https://www.science.org.au/curious/technology-future/lithium-ion-batteries

Energizer Brands, LCC (2020, December 1). Nickel Metal Hydride (Ni-MH). *Energizer Metal Hydride*. https://data.energizer.com/PDFs/nickelmetalhydride_app man.pdf

Hymel, S (2020, November 15). *What is a Battery?* SparkFun. https://learn.sparkfun.com/tutorials/what-is-a-battery/all

Karami, N., & Tabaray, J. (2015, April). Nickel Metal Hydride: Structure, Chemical Reaction,

and Circuit Model. https://ieeexplore.ieee.org/xpls/abs_all.jsp?arnumber=7113594

Libretexts. (2020, July 17). *1.1: Galvanic Cells.* https://chem.libretexts.org/Courses/University_of_California_Davis/UCD_Chem_002C/UCD_Chem_2C:_Larsen/Text/Unit_1:_Electrochemistry/1.1:_Galvanic_Cells

Molkov, V., Pollett, et. all (n.d.). Fuel-cell (hydrogen) electric hybrid vehicles.

ReLiON, (2015, October 19). *The Seven Top Uses For Rechargeable Lithium-Ion Batteries.* Blog.
https://relionbattery.com/blog/the-seven-top-uses-for-rechargeable-lithium-ion-batteries

Vassal, N., Salmon, E., & Favarque, J.-F. (1999). Nickel/Metal Hydride Secondary Batteries Using an Alkaline Solid Polymer Electrolyte. Journal of The Electrochemical Society, 146 (1) 20-26.https://citeseerx.ist.psu.edu/viewdoc/download?doi=10.1.1.905.8258&rep=rep1&type=pdf